



Wave glider observations of pCO₂ and upwelling dynamics in the Monterey Bay during the spring 2012 CANON experiment

Michael Fong, University of California, Berkeley

Mentors: Francisco Chavez and Gernot Friederich

Summer 2012

Keywords: wave glider, pCO₂, CANON experiment, upwelling

ABSTRACT

During the spring 2012 CANON experiment, the deployment of a wave glider instrument package, in the Monterey Bay, consisting of a CTD, oxygen sensor, pH sensor, CO₂ gas analyzer, and a weather station demonstrated the capability of the platform to reliably measure a host of parameters, including sea surface pCO₂. Comparison of pCO₂ measurements across multiple platforms showed excellent agreement and validated the wave glider method. Wave glider pCO₂ measurements during the strong spring upwelling provided unique observations of sea pCO₂ (>1000 ppm) and CO₂ flux in a region of strong winds (>20 m/s), where ship observations are sparse and unpractical. The high spatiotemporal resolution of the observations revealed complicated dynamics of the fate of upwelled pCO₂, which were further explored with a coupled biological and CO₂ flux model. Simulations of pCO₂ decay during the relaxation of upwelling demonstrated that a combination of biology and gas exchange was involved in lowering pCO₂ levels to atmospheric levels or below. Comparison of modeled decay timescales to advective timescales may explain some of the spatial variability in pCO₂ observed in the bay and point to preliminary insights and routes for further study.

INTRODUCTION

Sea surface carbon observations are important for quantifying the uptake of atmospheric CO₂, monitoring changes in ocean carbon chemistry due to anthropogenic CO₂ emissions, and estimating the air-sea CO₂ flux and has far-reaching implications for policy and decision making.

Currently, the majority of surface sea pCO₂ observations are from ship-based platforms, through ships of opportunity (SOOP) and voluntary observing ships (VOS), or from fixed station time series, such as the Bermuda Atlantic Time Series (BATS), the Hawaii Ocean Time Series (HOTS), and Ocean Station PAPA in the northeast Pacific (Monteiro *et al.*, 2009). Even after 50 years of CO₂ observations, there remain many observational deficiencies—large unsampled regions in the ocean and few regions with year-round monthly measurements (Monteiro *et al.*, 2009; Wilcox *et al.*, 2009). The low frequency of measurements is the cause of a seasonal bias in CO₂ flux estimates, which, if corrected, would improve the uncertainty from 40-50% to 10-15% (Monteiro *et al.*, 2009). High spatiotemporal resolution measurements are especially needed in coastal regions, where carbon chemistry and pH exhibit large spatiotemporal variability: for instance, a seasonal pH range of 0.1 at Station PAPA (same as the pH change over the last 200 years) (Wilcox *et al.*, 2009). Understanding long-term changes thus requires an understanding of the short-term variability.

Wave gliders have recently joined the fleet of sea surface carbon observing platforms and show promising potential for addressing the existing observational deficiencies. The wave glider is an autonomous surface vehicle, developed by Liquid Robotics, that operates by the wave-powered propulsion of a submerged glider, which tows the surface float along (Manley and Wilcox, 2010). Wave gliders offer the advantage of being low cost (compared to ship or mooring-based platforms), solar-powered, a persistent surface presence, capable of long range (>2500 mi.) and duration deployments (up to 1 yr.), and durable in rough sea conditions (up to 20 ft. seas and 50 kt. winds) (Manley and Wilcox, 2010; Liquid Robotics). For sea surface carbon observations, the long range and duration capabilities of the wave glider are especially valuable for sampling large swaths of the ocean and providing a continuous year-round presence. Furthermore, wave gliders can provide coverage of areas beyond the densely sampled shipping lanes, where the majority of the carbon observations are limited to. Wave gliders are already in use by NOAA PMEL for measuring sea surface pCO₂ and pH. Thorough validation of the wave glider sensors is necessary before the technology can become widely used for sea surface carbon observations.

The wave glider has been used at MBARI in the Controlled, Agile, and Novel Observing Network (CANON) experiments. A key premise of the CANON initiative is to attain better understanding of dynamics of the microbial food web and the biological pump through the

improvement of ocean observation capabilities at relevant spatiotemporal scales (MBARI, 2010). The most recent deployment of the wave glider was in the Monterey Bay from late May to early June as part of the spring 2012 CANON experiment. During its spring deployment, the wave glider collected high frequency observations of pCO₂, pH, and other chemical and physical parameters during a strong upwelling event. The objective of this study was to analyze the wave glider observations to assess the capability of the platform in capturing the seasonal upwelling dynamics and the spatiotemporal variability of surface sea pCO₂ in the Monterey Bay, investigate the processes that regulate sea pCO₂, and validate the wave glider pCO₂ platform.

MATERIALS AND METHODS

WAVE GLIDER PLATFORM:

The wave glider hosted a variety of instruments from MBARI's Ocean Acidification (OA) moorings. Integration of the OA instrumentation into the wave glider platform by Tougher (unpublished, 2011) resulted in the capability to monitor a suite of parameters at the surface: temperature, salinity, oxygen, pH, and pCO₂. Instruments mounted on the hull included a Seabird Payload Glider CTD, a SBE-43 dissolved oxygen sensor, and a Honeywell Durafet II pH electrode. An Airmar PB-200 weather station was fixed 1 m above the glider and provided measurements of instantaneous wind speed, wind direction, relative humidity, and air temperature. The pCO₂ system was integrated into the aft drybox and consisted of a Licor-820 non-dispersive infrared CO₂ gas analyzer. A CO₂ standard tank of 380 µatm was used to monitor precision and accuracy. Surface sea pCO₂ was determined by measuring the CO₂ in dry, CO₂-free air equilibrated with the seawater sample. Soda lime in the valve block served as a CO₂ scrubber and a dessicator, to obtain dry, CO₂-free air.

STUDY SITE:

During the spring CANON experiment, the wave glider operated in conjunction with a host of various ocean observation platforms. For this study, wave glider data was compared to data from the *Dorado* AUV, the M1 mooring, the *Fulmar* research vessel underway pCO₂ and CTD systems, and the *Fulmar* profiling CTD. The period of the wave glider observations was from May 22 to June 5. **Figure 1** shows the wave glider track, the *Fulmar* profiling CTD stations, and the *Fulmar* underway tracks.

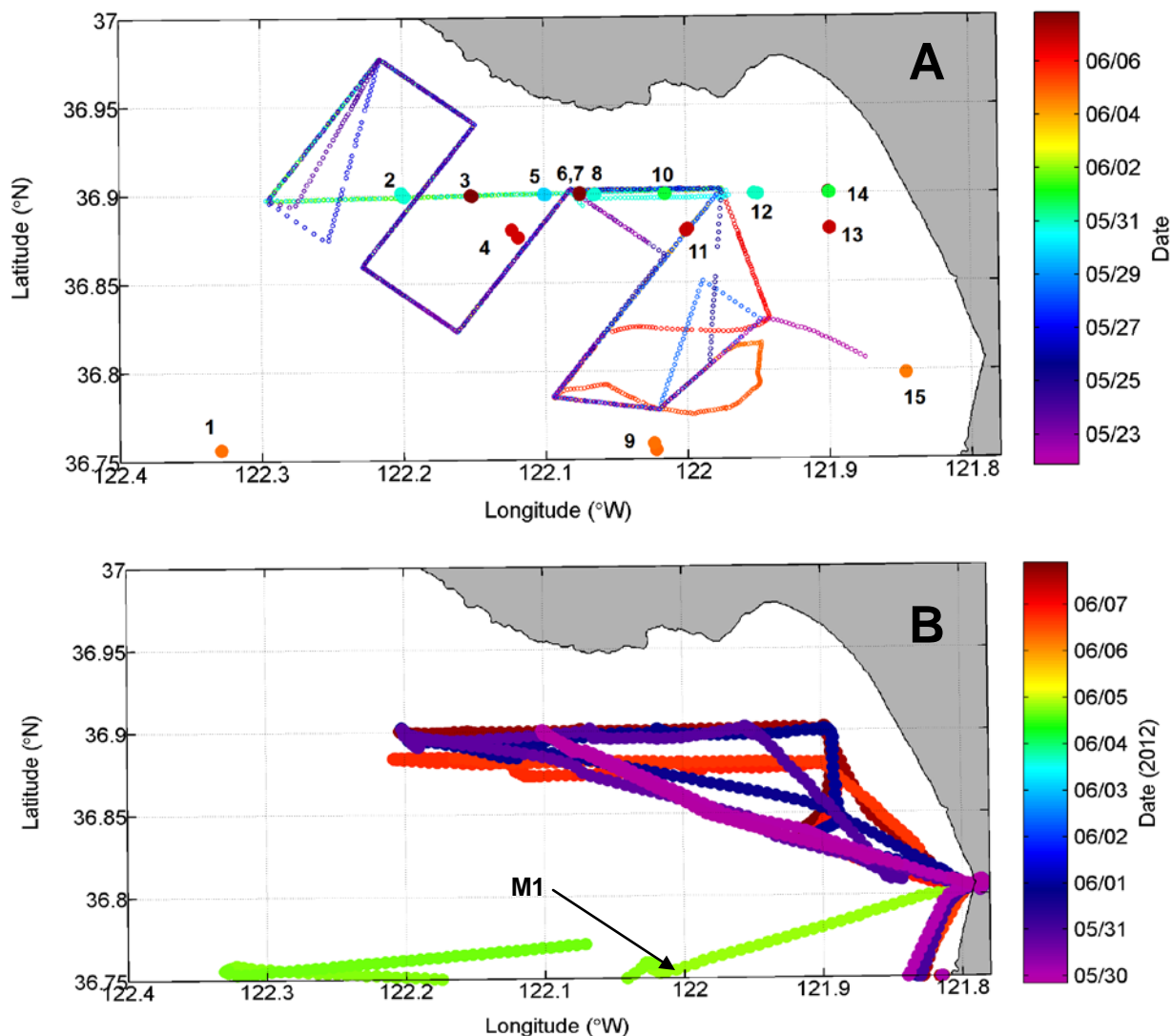


Figure 1: (A) Track of the wave glider (open circles) and the locations of the *Fulmar* profiling CTD stations (numbered, filled circles). The date of occupation is shown on the color axis. (B) Track of the *Fulmar* underway system, with date on the color axis. M1 is shown by the arrow.

WAVE GLIDER DATA:

For visualization, the wave glider data was divided into 10 legs, based on similar trajectories, and with each leg up to 3 days in duration. The legs, excluding those that only ran along 36.9°N, were gridded using the DIVA gridding algorithm in Ocean Data View. The wave glider took measurements for temperature, salinity, O₂, pH, pCO₂, and meteorological conditions every 10 minutes, but the measurement times were not synchronized between the weather station and the sea surface sensor package. To compare the meteorological and oceanographic data, hourly-averaged wind speeds were matched to the oceanographic measurements. Wind speeds

were normalized to the standard reference height of 10 m using the `wstress` Matlab function written by Rich Signell at the Woods Hole USGS, based on the formulation by Large and Pond (1981). Air-sea CO₂ and O₂ fluxes were calculated using the relationships given in Wanninkhof (1992).

pCO₂ COMPARISON ACROSS PLATFORMS:

For validation of the wave glider pCO₂ system, wave glider sea pCO₂ measurements were compared to sea pCO₂ measured from the M1 mooring station and the *Fulmar* underway. Wave glider pCO₂ (at the surface) were directly calibrated against M1 pCO₂ (at a depth of 1 m) values. Data points were matched in space and time to within less than 4 km. and 4 min. apart. M1 pCO₂ was calculated from the ΔpCO₂ measurements at the mooring as described in Friederich *et al.* (1995). Because direct calibration provided only a handful of matching data, a more meaningful comparison was pCO₂ in a temperature and salinity space (for data points within the same space and time domain). The *Fulmar* underway pCO₂ was compared only in a temperature space, because an erroneous offset was found between the *Fulmar* salinity measurements and that from the profiling CTD.

CO₂ measurements from the *Fulmar* underway system were given as xCO₂ (the mole fraction) at the measurement temperature and required conversion to pCO₂ at the in-situ temperature. The relationship between xCO₂ and pCO₂ is given by **Equation 1**, where P_{tot} is the total pressure and pH_2O is the partial pressure of water.

$$pCO_2 = xCO_2(P_{tot} - pH_2O) \quad (1)$$

The partial pressure of water is dependent on the in-situ temperature and salinity and was calculated by the relationship given by Weiss and Price (1980). The pCO₂ at the measurement temperature was converted to the pCO₂ at the in-situ temperature using the empirical relation found by Takahashi *et al.* (1993) (**Equation 2**).

$$pCO_2(T_{insitu}) = pCO_2(T_{meas}) * e^{(0.0423*(T_{insitu} - T_{meas}))} \quad (2)$$

pCO₂ DECAY MODEL:

The decay of pCO₂ during the relaxation of upwelling was simulated with a carbonate system model, developed by Friederich (unpublished) and based on the biological uptake of CO₂,

gas exchange, nutrient uptake, and Redfield ratio relationships. The model is described by **Equations 3-11**, and a dictionary of the variables is given in **Table 1**.

The macronutrients (nitrate, phosphate, silicate) affect pCO₂ through fueling primary productivity and affecting alkalinity (Wolf-Gladrow *et al.*, 2007) and thus the carbonate system. The macronutrient concentrations as a function of time, and the mutual dependence of chlorophyll (primary production) and the nutrients are described by **Equations 3-6**. The consumption of nitrate (**Equation 3**) is driven by new production (Eppley and Peterson, 1979), and the modeled increase in chlorophyll (**Equation 4**) is due only to new production (consumption of nitrate). Phosphate and silicate can be determined directly from the instantaneous in-situ nitrate concentrations via the Redfield ratio (**Equations 5,6**).

$$NO_3^-(t + dt) = NO_3^-(t) - (dt)\mu(chl(t)) \frac{NO_3^-(t)}{|NO_3^-(t)|+0.5} \quad (3)$$

$$chl(t + dt) = chl(t) + (NO_3^-(t) - NO_3^-(t + dt)) \quad (4)$$

$$PO_4^{3-}(t + dt) = \frac{NO_3^-(t+dt)}{16} + 0.2 \quad (5)$$

$$Si = NO_3^- \quad (6)$$

pCO₂ was determined from the dissolved inorganic carbon and the total alkalinity, through routine carbon system calculations using the CDIAAC CO2SYS program for Matlab. Dissolved inorganic carbon consumption (**Equation 7**) is due to biological consumption from new production (the nitrate terms), carbonate precipitation (estimated from the carbonate to organic carbon ratio), and loss of CO₂ to the atmosphere through air-sea flux (last term). The air-sea flux was calculated using the relationships given by Wanninkhof (1992). The total alkalinity decreases with carbonate precipitation and consumption of nitrate by new production (**Equation 8**).

$$TCO_2(t + dt) = TCO_2(t) + (1 + c_r)(NO_3^-(t) - NO_3^-(t + dt))(r_{CN}) - \frac{dt}{MLD} * F(i) * 1000 \quad (7)$$

$$TA(t + dt) = TA(t) - (NO_3^-(t) - NO_3^-(t + dt))(2c_r r_{CN}) \quad (8)$$

$$pCO_2(t + dt) = pCO_2(T(t + dt), S(t + dt), TA(t + dt), TCO_2(t + dt), PO_4^{3-}(t + dt), Si(t + dt)) \quad (9)$$

The cumulative loss of CO₂ to the atmosphere by air-sea flux can be calculated by integrating the CO₂ flux over time (**Equation 10**). The growth in particulate organic carbon can

be inferred from the difference between cumulative change in DIC (**Equation 11**) and the cumulative atmospheric loss of CO₂ (**Equation 10**).

$$F_{cum}(t + dt) = F(t + dt) * dt + F_{cum}(t) \quad (10)$$

$$dTCO_2(t + dt) = 12(TCO_2(0) - TCO_2(t + dt)) \frac{MLD}{1000} \quad (11)$$

Table 1: Dictionary of variables and constant values used in the pCO₂ decay model

Variable	Description	Units	Constant value
dt	time step	days	0.01
t	time	days	--
NO_3^-	nitrate	μM	--
chl	chlorophyll a	mg m ⁻³	--
PO_4^{3-}	phosphate	μM	--
μ	growth rate		--
Si	silicate	μM	--
TCO_2	dissolved inorganic carbon	μM	--
c_r	ratio of carbonate to inorganic carbon	--	0
r_{CN}	carbon to nitrogen Redfield ratio	--	6.8
MLD	mixed layer depth	m	10
$F(i)$	sea to air CO ₂ flux	mol m ⁻² d ⁻¹	--
TA	total alkalinity	μM	--
T	temperature	°C	--
S	salinity	psu	--
F_{cum}	cumulative sea to air CO ₂ flux (cumulative loss of CO ₂ to the atmosphere)	g m ⁻²	--
$dTCO_2$	cumulative change in DIC	g m ⁻²	--
pH	pH (seawater scale)	--	--
K_1, K_2	dissociation constants for H ₂ CO ₃ and HCO ₃ ⁻	--	Roy et al., 1993
K_{SO4}	dissociation constant for HSO ₄ ⁻	--	Dickson, 1990

Simulations were performed at four different stations (**Table 2**). M1 was the only mooring station, while the other three stations were virtual mooring stations with data obtained from repeat occupations by the wave glider. F2 and F10 corresponded with the *Fulmar* profiling CTD stations 2 and 10 (**Figure 1A**). WG was the northernmost point occupied by the wave glider and first saw the highest sea pCO₂ water from the source upwelled water before being

advected southwards. F2 and M1 lied in the path of the upwelling plume, and F10 was the inner bay station.

Five simulations total were performed at the four different stations with the initial conditions given in **Table 3**. A zero growth rate scenario was modeled at WG in addition to a constant growth rate scenario. Initial nutrient concentrations were based on an assumed high initial nitrate concentration of 30 μM , typical of upwelled waters. Initial chlorophyll in the outer bay stations was assumed to be low (0.5 mg m^{-3}), except for F2 where bottle chlorophyll data showed that the initial concentration was 5 mg m^{-3} . Because inner bay waters are typically more productive, the initial chlorophyll was assumed to be 5 mg m^{-3} as well. As a crude approximation for growth rate, the growth rate that resulted in a pCO_2 decay that most closely matched the observations was used throughout the simulation. At F2, the growth rate was estimated from the change in chlorophyll from two different samplings, using the exponential growth relation $\mu = \frac{1}{\Delta t} \ln \left(\frac{\text{chl}(\Delta t)}{\text{chl}(0)} \right)$. Initial TCO_2 was assumed to be $2100 \mu\text{M}$ (average ocean value). Initial pCO_2 was from observational data. Temperature, salinity, and wind speed were all derived from observational data and interpolated between data points to obtain values for each time step of the simulation. If the simulation ran beyond the duration of the observations, the temperature, salinity, and wind speed were held constant at the last value for the remaining duration of the simulation.

Table 2: Positions of the stations evaluated with the pCO_2 decay model

Station	Latitude ($^{\circ}\text{N}$)	Longitude
WG	36.98	-122.22
F2	36.9	-122.2
F10	36.9	-122.02
M1	36.75	-122.03

Table 3: Initial conditions and inputs of the model simulations

	WG	F2	F10	M1
NO_3^-	30	30	30	30
Si	30	30	30	30
PO_4^{3-}	2.1	2.1	2.1	2.1
chl	0.5	5	5	0.5
μ	0,0.3	0.69	0.4	0.45
pCO_2	1150	1078	412	943
TCO_2	2100	2100	2100	2100
T	9.0	9.6	10.5	9.3
S	33.97	33.93	33.8	33.9
wind speed at 10m (m/s)	8.3	8.5	15.1	16.4

RESULTS

STRONG SPRING UPWELLING EVENT:

From satellite SST imagery (**Figure 2**), upwelling along the central California coast began on May 20 and reached its peak by May 25, with SSTs dropping as low as 9°C in the outer Monterey Bay. Slow relaxation of the upwelling then followed, with outer bay SSTs warming to 12°C nine days later.

Comparison of instantaneous wind speeds from the wave glider weather station to the wave glider SSTs showed strong longshore winds, with the strongest winds being >20 m/s, during the upwelling and then a progressive weakening of winds during upwelling relaxation (**Figures 3, 5-14**).

At the M1 station, sea pCO₂ reached a historical record high of approximately 1000 µatm at the peak of the upwelling, and then slowly decayed back to initial concentrations (500 µatm) over the same timescale of relaxation as observed from SST (**Figure 4**).

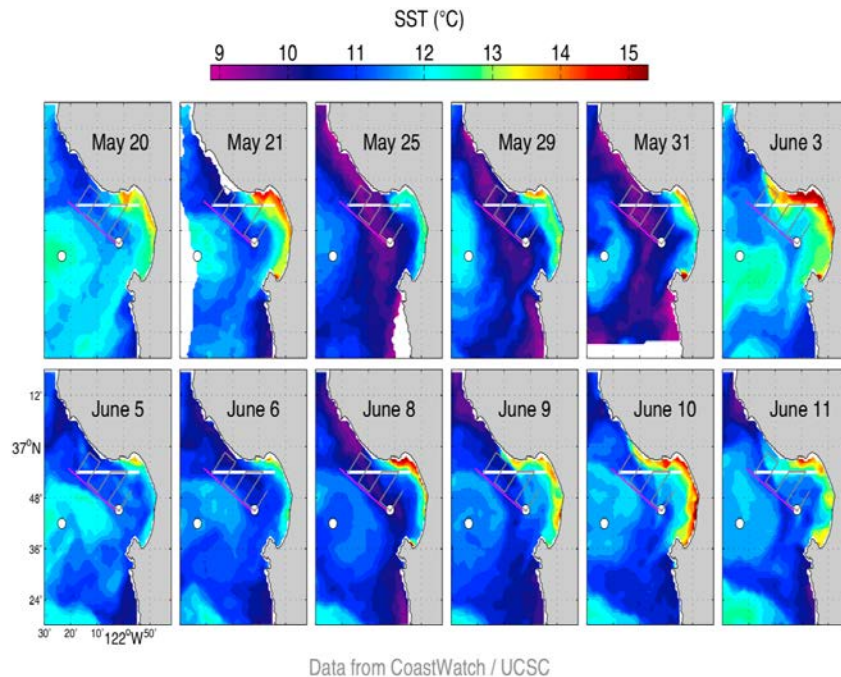


Figure 2: Sea surface temperature from satellite imagery showing the upwelling and relaxation from May 20 – June 11.

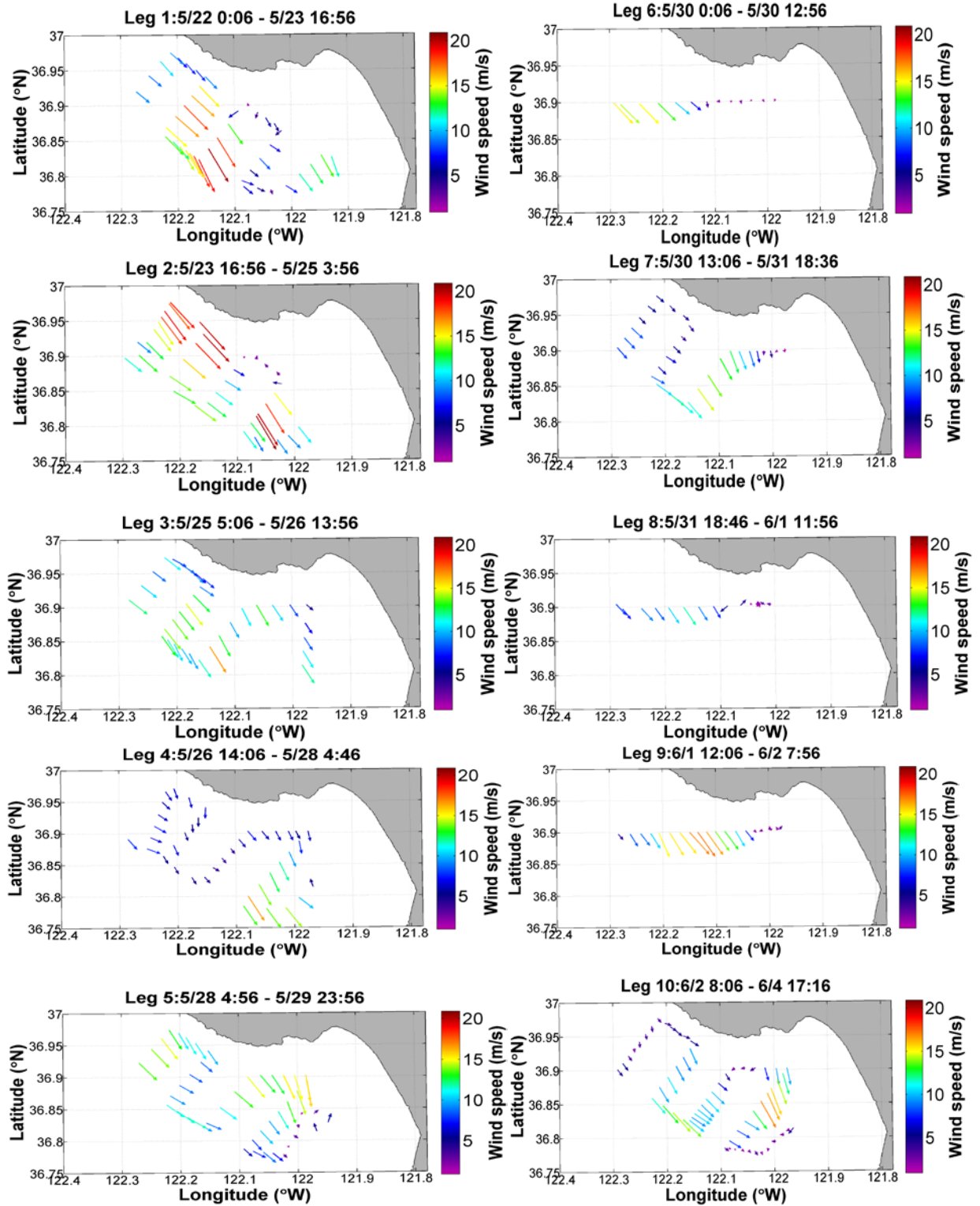


Figure 3: Wind speed (normalized to a reference height of 10 m) and direction, measured by the wave glider weather station, in each of the ten legs. Length and color of the arrows denote wind speed (m/s). The first leg (upper left corner) starts on May 22 and the last leg ends on June 4.

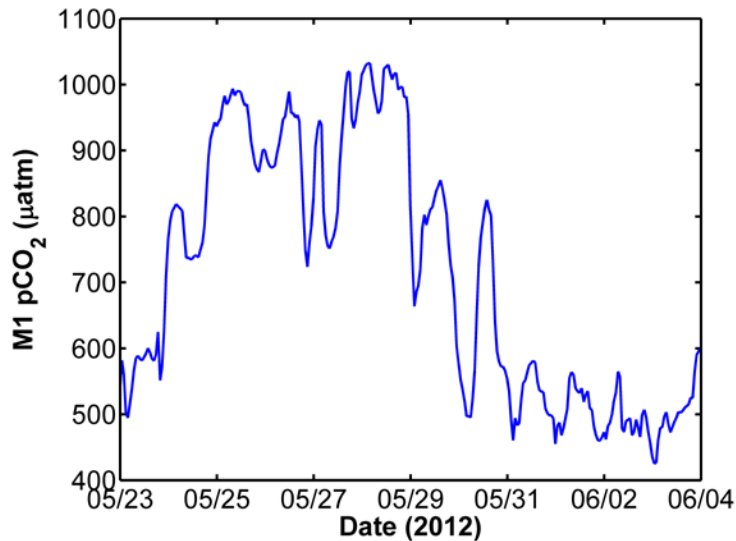


Figure 4: Time series of sea $p\text{CO}_2$ at a depth of 1 m at the M1 mooring station during the wave glider observation period (May 23 – June 4).

WAVE GLIDER OBSERVATIONS:

The upwelled water first appeared in leg 1 at the northernmost tip of the observation domain, near Davenport, CA, as evident in the characteristic low temperature and high salinity signature (9°C , 33.9 psu) (**Figure 5**). The upwelled water quickly advected southward and, by leg 3, the upwelling reached its peak (9°C , 34 psu) (**Figure 7**). By leg 10, as the upwelling relaxed over the next 9-10 days, SSTs gradually warmed up to an average of 11°C and the saline waters (33.9 psu) spread to most of the observation region (**Figure 14**).

The upwelled water also had characteristically high $p\text{CO}_2$, low pH, and high O_2 , with the most extreme values seen in leg 3 ($1200 \mu\text{atm } p\text{CO}_2$, $100 \mu\text{M } \text{O}_2$, $\text{pH} = 7.6$) (**Figure 7**). With the relaxation of upwelling, $p\text{CO}_2$ gradually decreased and was at atmospheric levels ($400 \mu\text{atm}$) throughout most of the observation region by leg 10; O_2 increased to $200 \mu\text{M}$, and pH increased to 8 (**Figure 14**). However, despite these observed temporal variabilities, several spatial features were persistent throughout the observation period. Sea $p\text{CO}_2$ was persistently below atmospheric levels in the inner bay region, reaching as low as $200 \mu\text{atm}$, while the $p\text{CO}_2$ in the outer bay was persistently above atmospheric levels, at least $600 \mu\text{atm}$ (**Figures 5-14**). Similar trends were observed for O_2 and pH—persistently higher O_2 and pH in the inner bay and lower O_2 and pH in the outer bay.

Leg 1 5/22 0:06 - 5/23 16:56

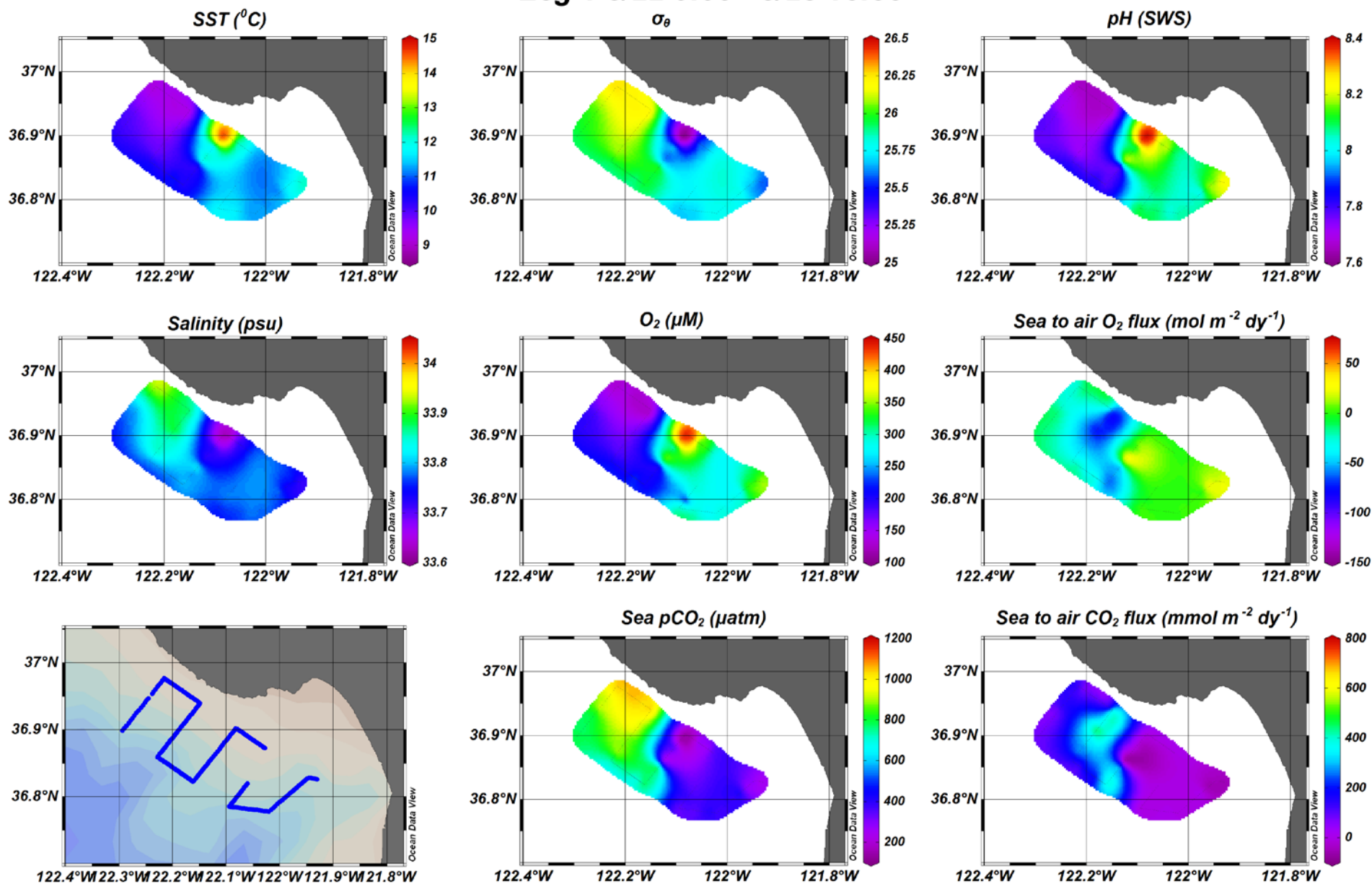


Figure 5: Leg 1 of the wave glider observations. From top left corner, going down, are sea surface temperature, salinity, the glider track, potential density, dissolved oxygen, sea pCO_2 , pH (seawater scale), sea to air O_2 flux, and sea to air CO_2 flux. The data were gridded using the DIVA gridding algorithm from Ocean Data View.

Leg 2: 5/23 16:56 -5/25 3:56

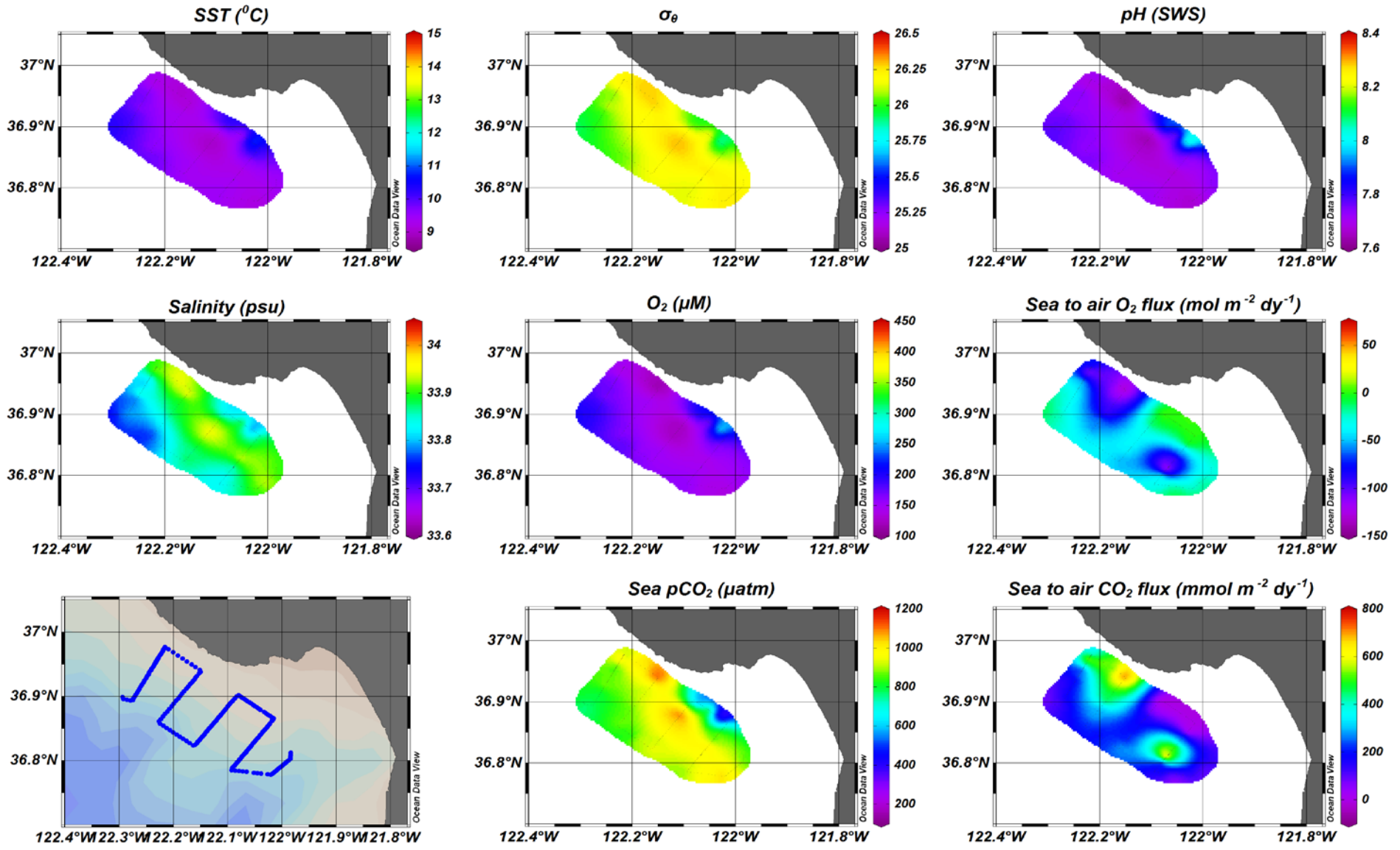


Figure 6: Leg 2 of the wave glider observations.

Leg 3 5/25 5:06 - 5/26 13:56

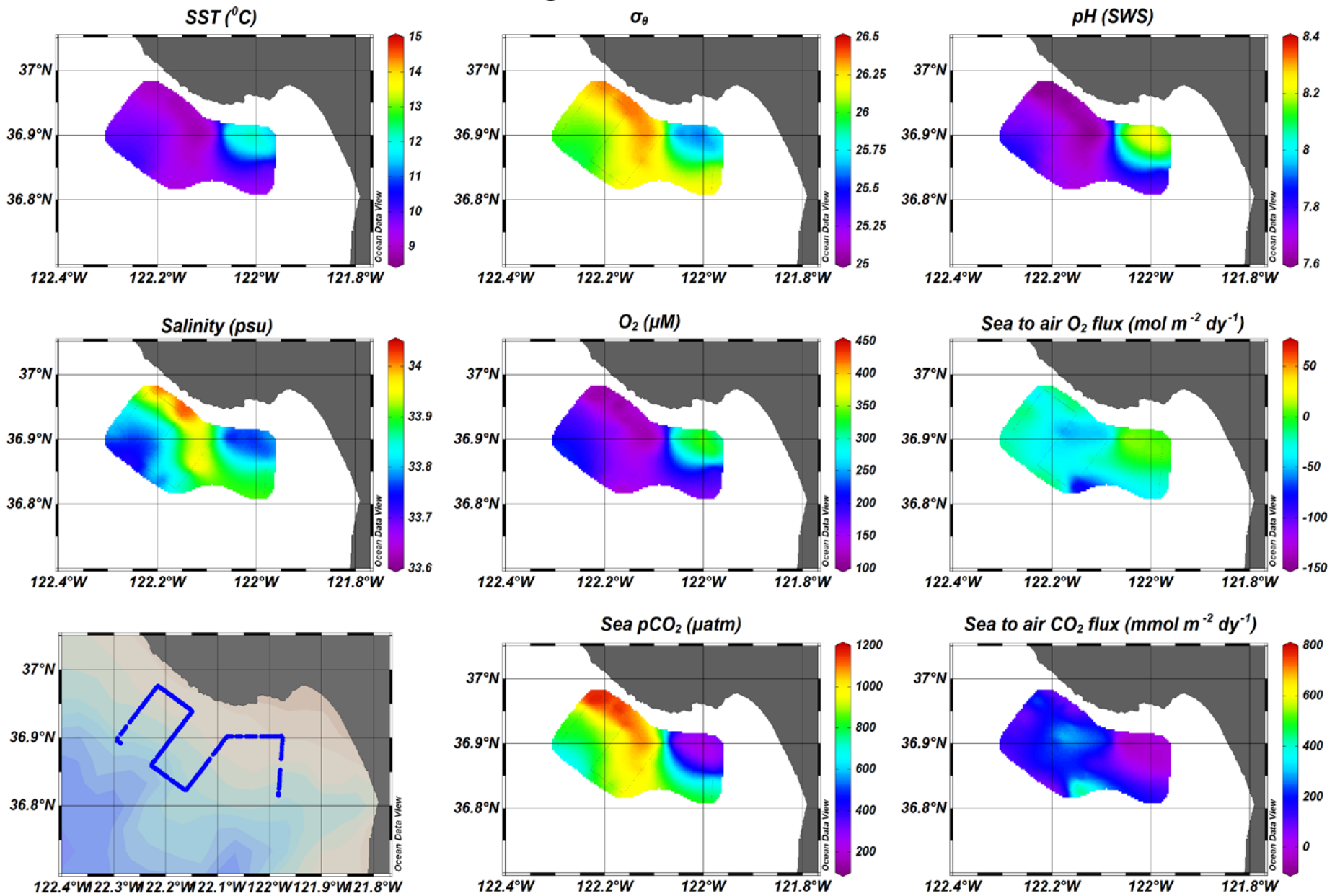


Figure 7: Leg 3 of the wave glider observations.

Leg 4 5/26 14:06 - 5/28 4:46

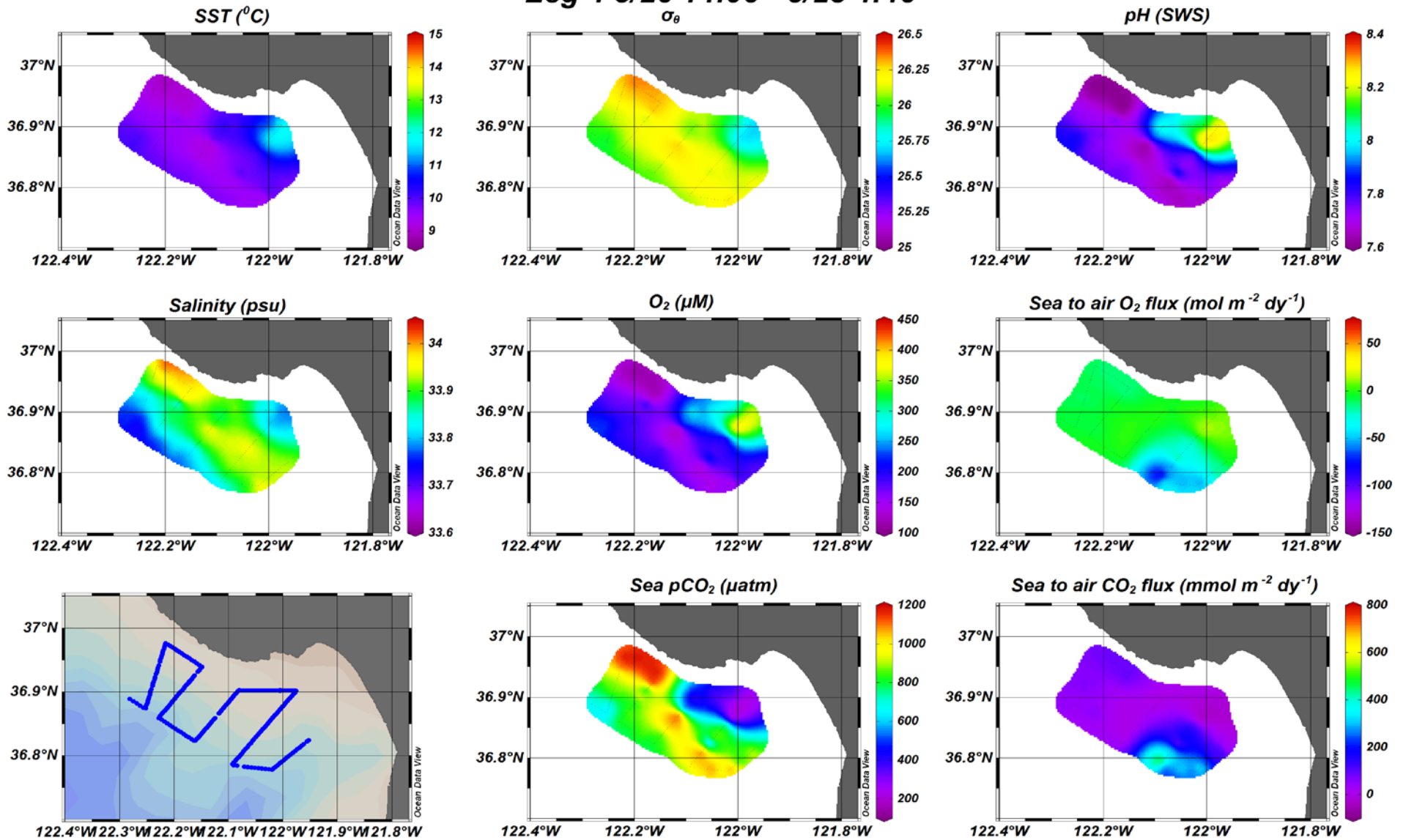


Figure 8: Leg 4 of the wave glider observations

Leg 5 5/28 4:56 - 5/29 23:56

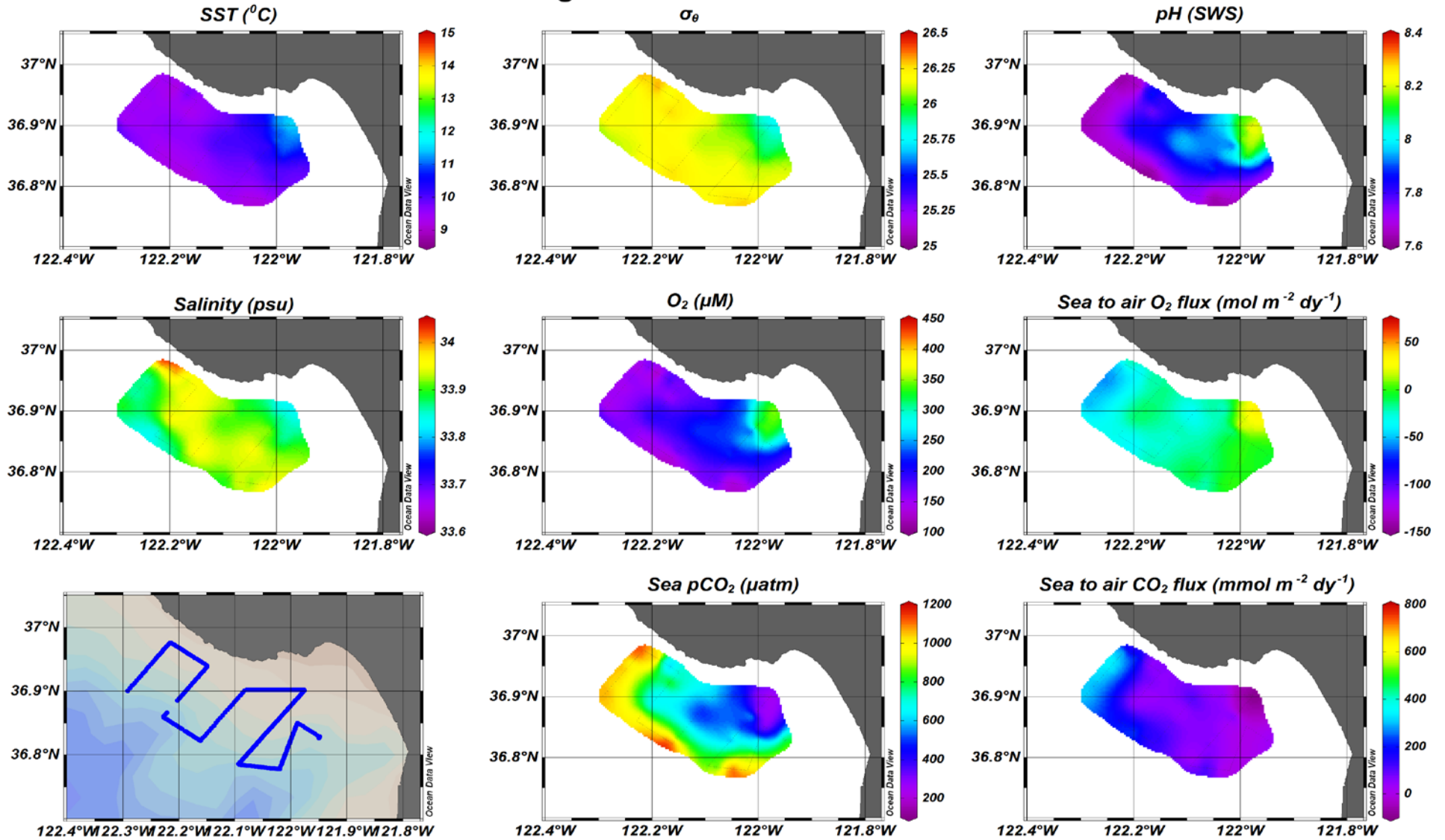


Figure 9: Leg 5 of the wave glider observations.

Leg 6 5/30 0:06 - 5/30 12:56

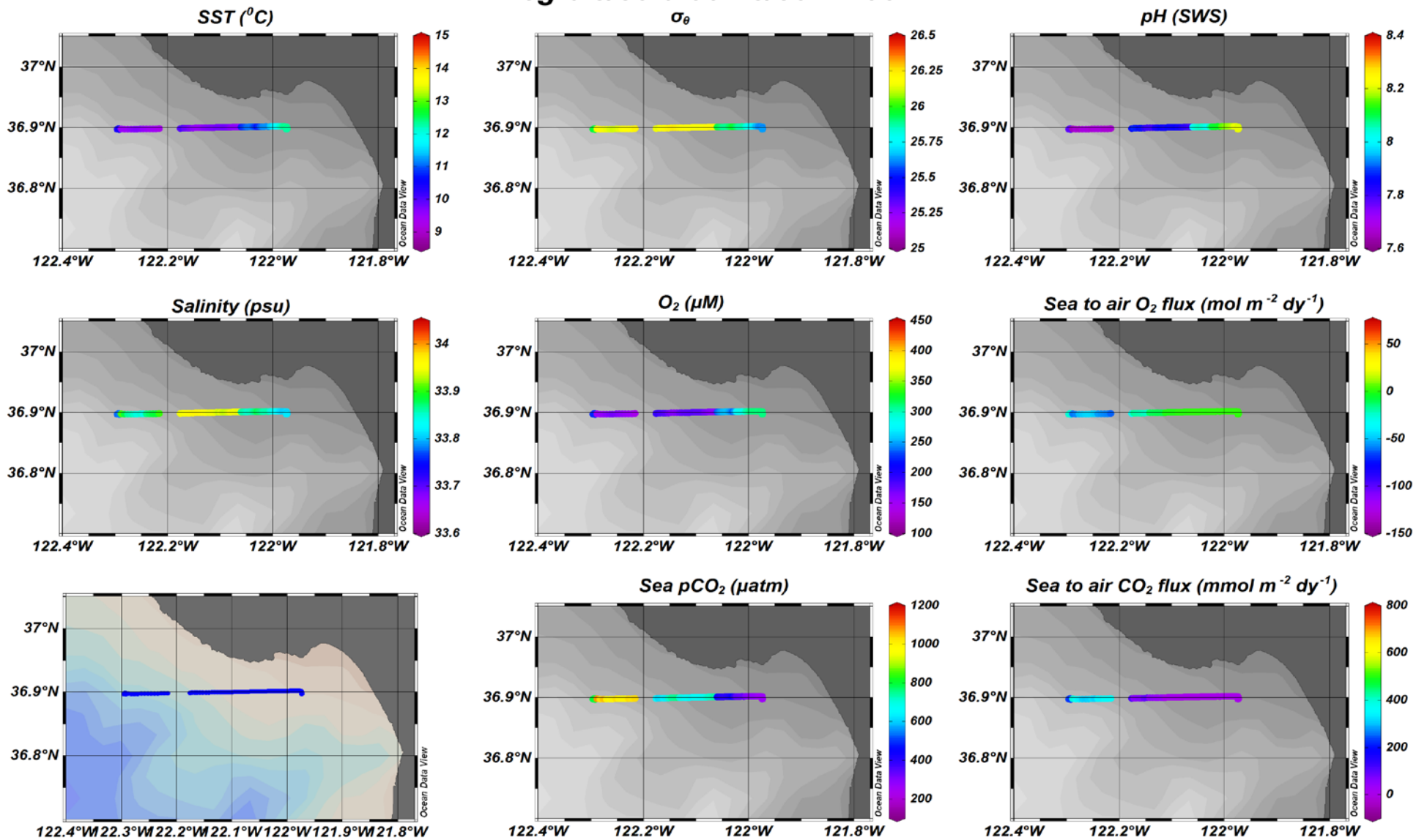


Figure 10: Leg 6 of the wave glider observations.

Leg 7 5/30 13:06 - 5/31 18:36

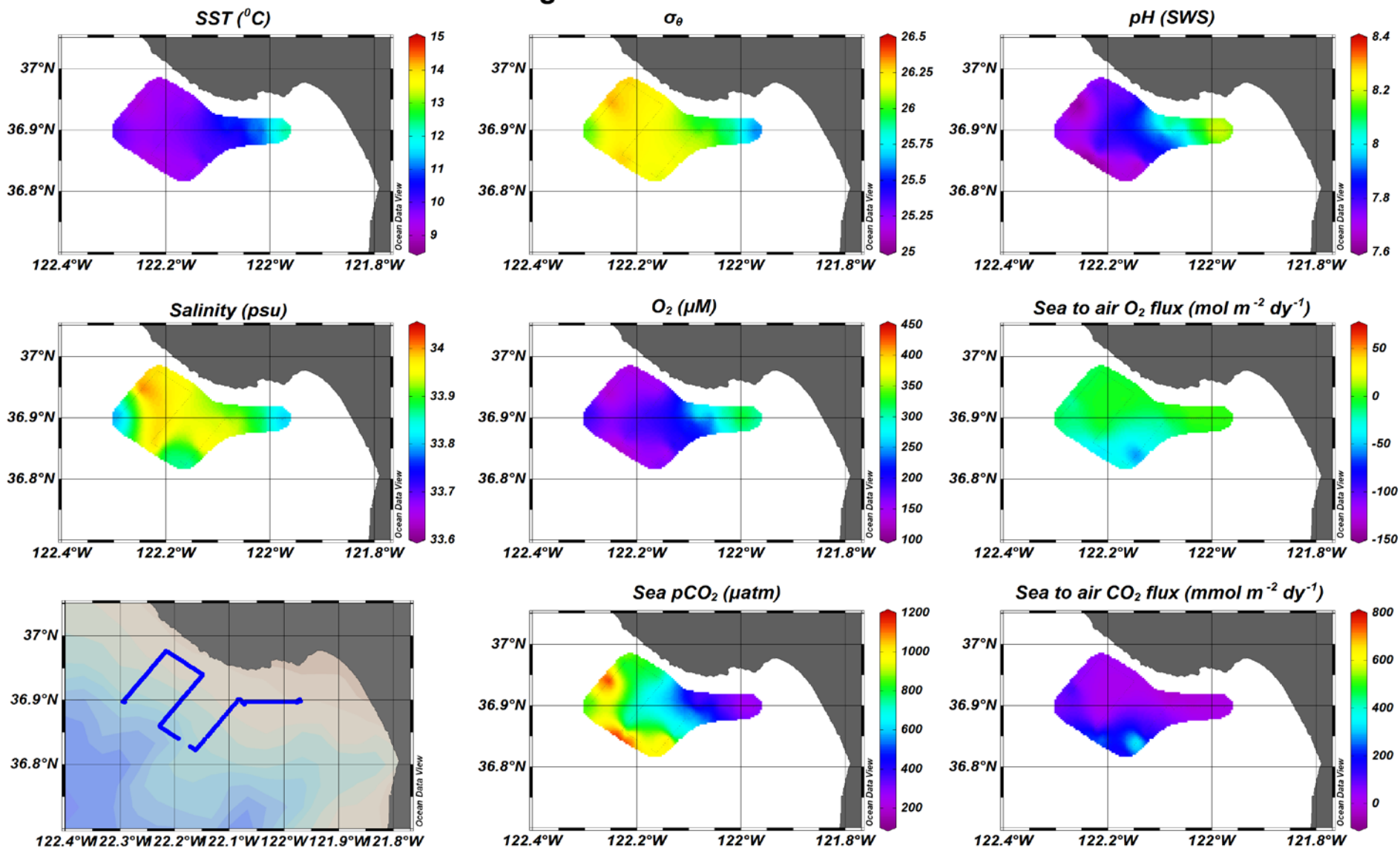


Figure 11: Leg 7 of the wave glider observations.

Leg 8 5/31 18:46 - 6/1 11:56

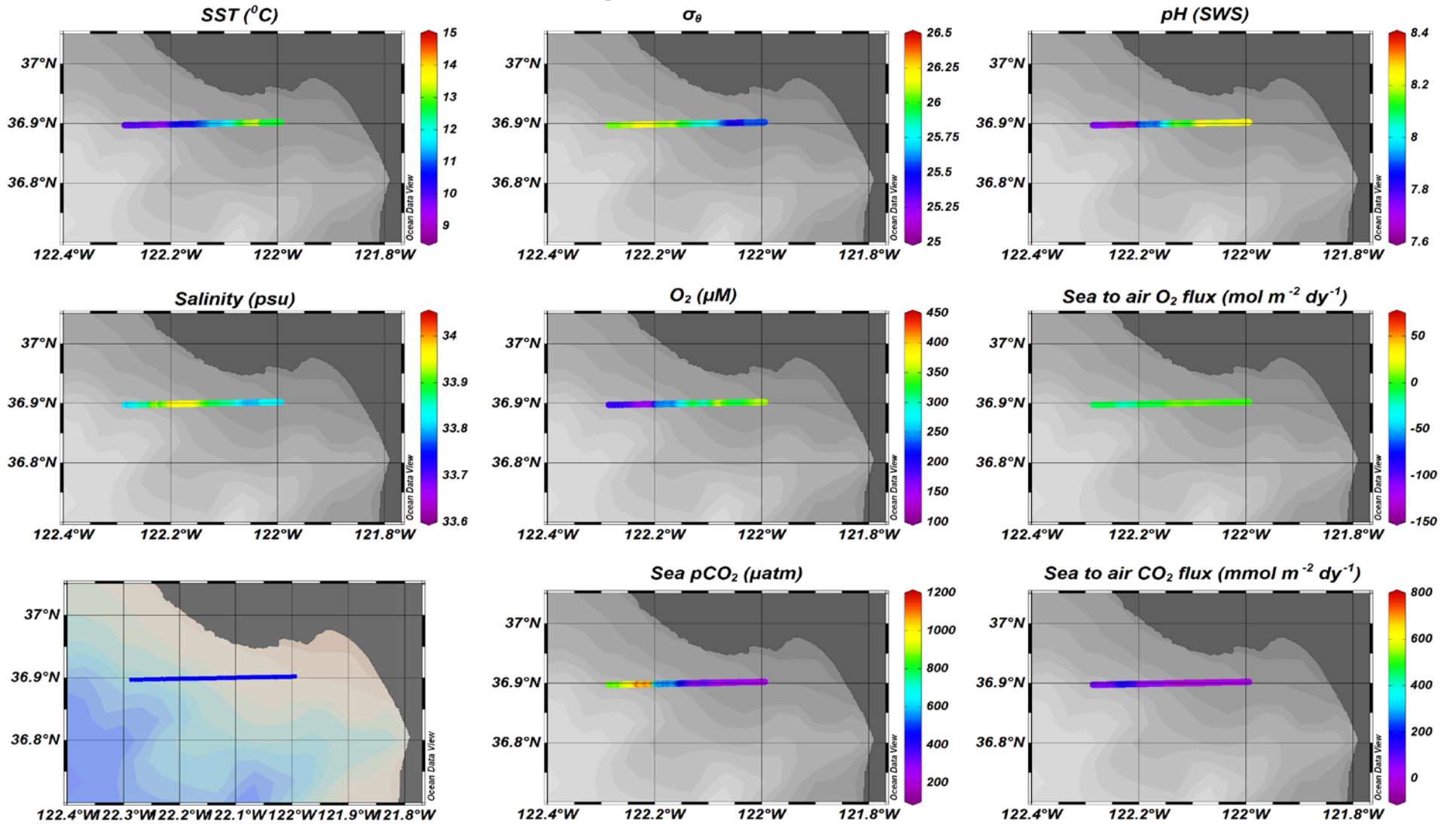


Figure 12: Leg 8 of the wave glider observations.

Leg 9 6/1 12:06 - 6/2 7:56

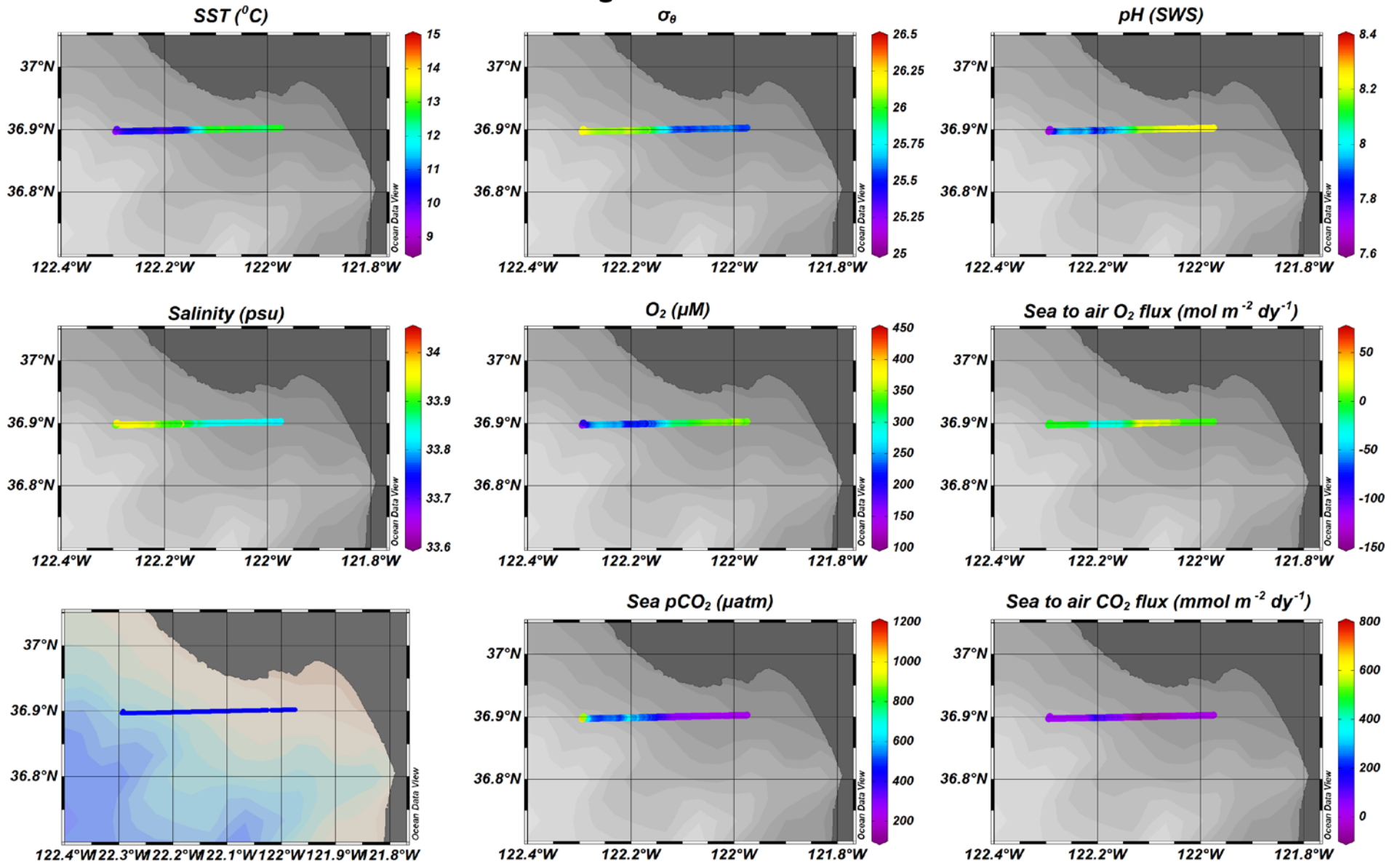


Figure 13: Leg 9 of the wave glider observations

Leg 10 6/2 8:06 - 6/4 17:16

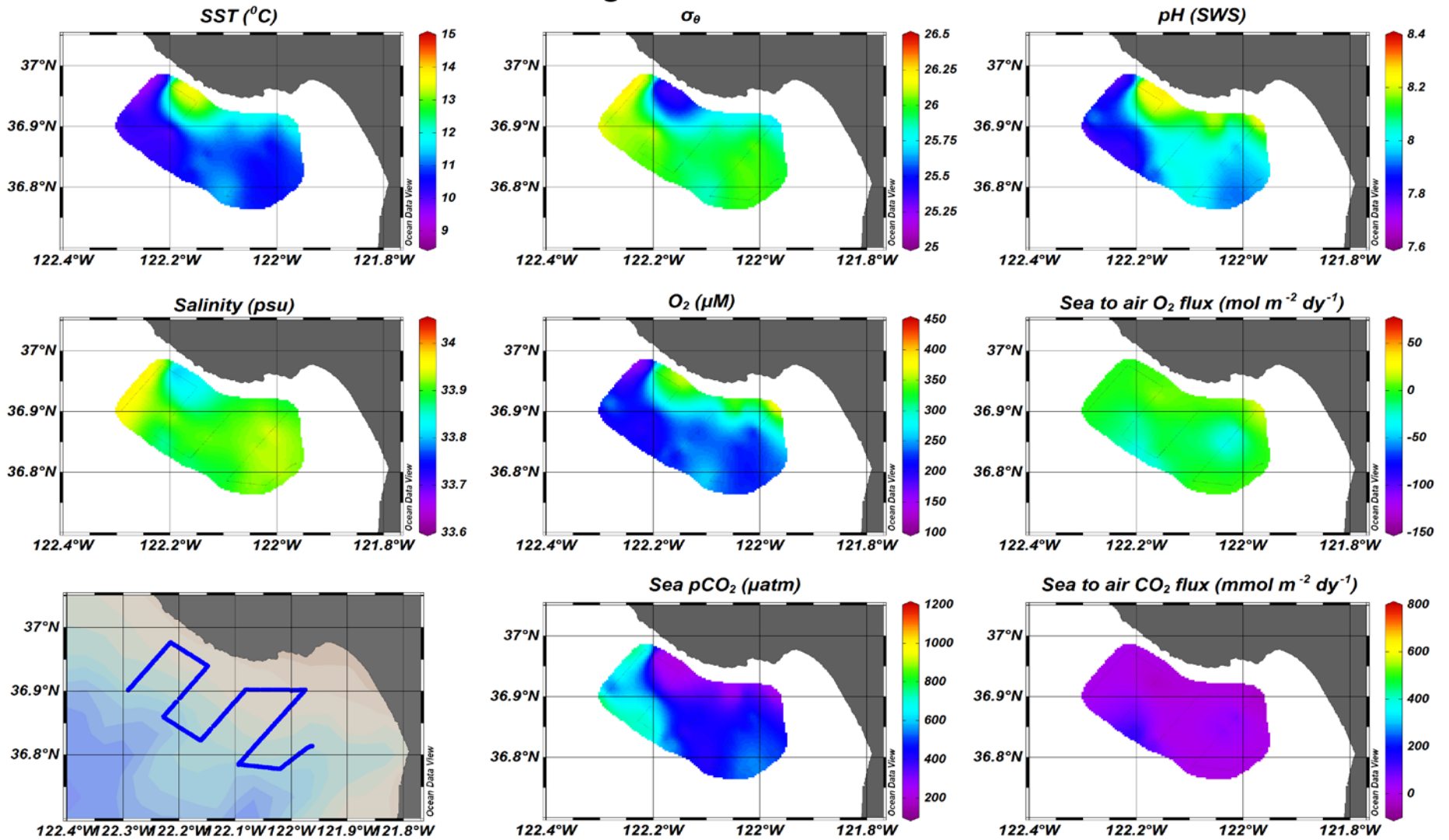


Figure 14: Leg 10 of the wave glider observations

SHARP SPATIAL AND TEMPORAL GRADIENTS:

Wave glider observations revealed sharp spatial and temporal gradients in $p\text{CO}_2$ and pH. Along the 36.9°N transect, $p\text{CO}_2$ gradients of $800 \mu\text{atm}$ were frequently observed over 31 km, and the sharpest $p\text{CO}_2$ gradient was a change of $600 \mu\text{atm}$ over a distance of less than 4 km (**Figure 15A**). The same pattern of gradients was observed in pH (**Figure 15B**). Sharp temporal gradients were also observed. In one instance, the $p\text{CO}_2$ time series of multiple wave glider occupations at the Fulmar CTD station 2 saw a $p\text{CO}_2$ decrease of $550 \mu\text{atm}$ on the order of hours (**Figure 16**).

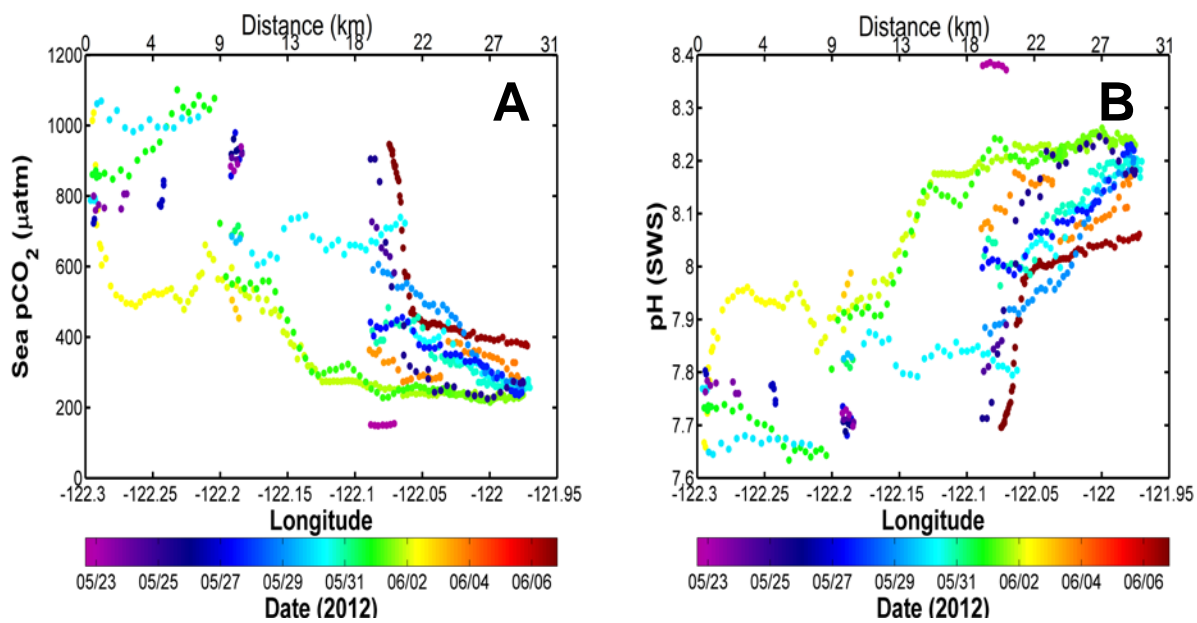


Figure 15: Wave glider measured sea $p\text{CO}_2$ (A) and pH (B) along 36.9°N , with date of occupation on the color axis.

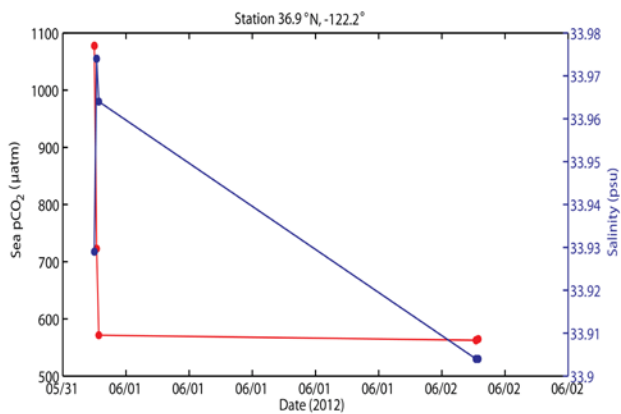


Figure 16: Wave glider occupations at the Fulmar CTD station 2 (36.9°N , -122.2°) showing the sea $p\text{CO}_2$ (red) time series with corresponding salinities (blue).

OBSERVATIONS OF WATER MASSES AND MIXING REGIMES:

A temperature-salinity (TS) plot of the wave glider observations revealed three major water masses and the mixing pathways among the three end members (**Figure 17A**). Comparison of the TS signatures of the end members with surface maps of temperature and salinity showed that the three major water masses observed were the inner bay water (warm, low salinity), the upwelled water (cold, high salinity), and the offshore water (cold, low salinity) (**Figure 17B**).

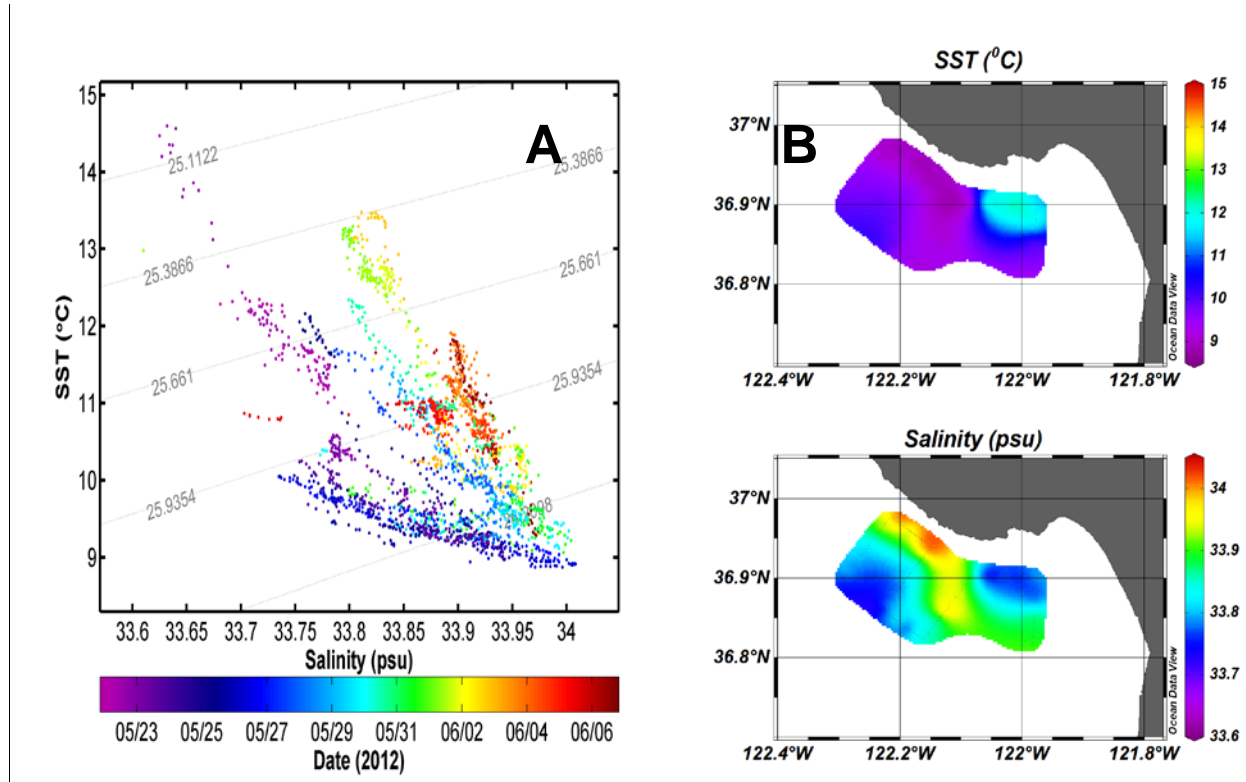


Figure 17: (A) TS plot of the wave glider data, with density contours, and data points colored by date. The TS plot shows the signatures of the major water masses and also intermediate products of mixing. (B) SST and salinity observed by the wave glider in Leg 3, showing the positions of the major water masses.

The wave glider observations captured well the intermediate products of mixing, as seen in the well-defined mixing lines in **Figure 17A**, and they also captured well the time evolution of mixing, showing the changing slopes of the mixing lines with the warming and spreading of saline waters during the relaxation of upwelling. At the beginning of the observation period (May 22), mixing was predominantly between an ephemeral warm, low salinity water mass (14.5°C, 33.66 psu) and the early stage of the upwelled water (purple mixing line, **Figure 17A**). By the peak of upwelling (5/25-5/26), the mixing line shifted to that between the offshore and

upwelled water (blue), which had a characteristic signature of 9°C, 34 psu. Mixing between the upwelled water and the inner bay water was also seen, and this mixing line increased in slope over time as the inner bay water gradually warmed and increased in salinity due to the intrusion of the saline, upwelled waters (**Figure 17A**).

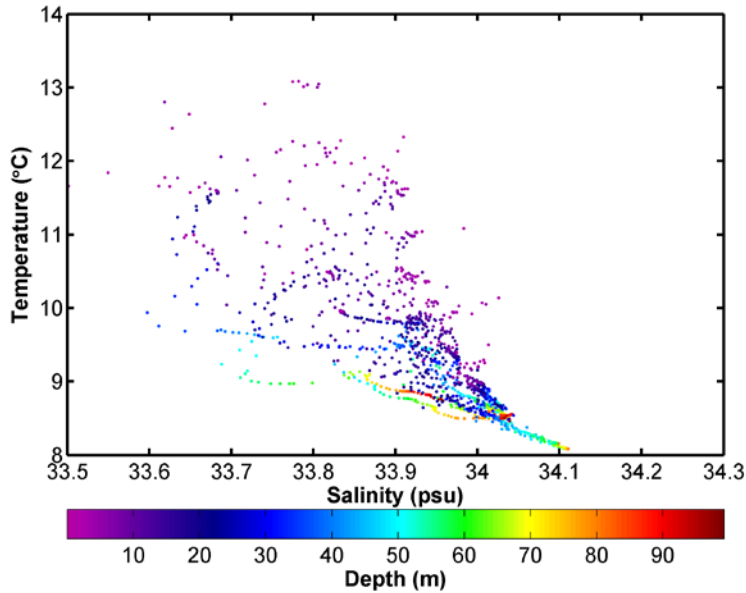


Figure 18: TS plot of Fulmar CTD casts (for ≤ 100 m) during the same observation period as the wave glider. The depth of the water mass is shown by color.

A TS plot of Fulmar profiling CTD casts during the same observation period, for depths up to 100 m, showed temperature and salinity values within the same range of values observed by the wave glider, but distinct mixing lines were not apparent (**Figure 18**). However, the subsurface sampling by the CTD revealed that the source of the upwelled water is from a depth of 30-50 m (**Figure 18**).

The mixing regime observed by the wave glider was corroborated by the same observations at the M1, WG, and F10 stations. A TS plot at M1 over the same observation period showed the transit of the three major water masses through the station (**Figure 19**). Initially, inner bay water was observed at M1 (purple). Three days later, the upwelled water reached M1 (blue). The quick upwelling was then followed by a slow relaxation: another 10 days before a mixture of upwelled and inner bay water (orange) appeared at M1 and then 2 more days before the initial inner bay water (red) returned to the location. At WG, initially the water mass was a

mixture of the offshore and upwelled end member (**Figure 20A**). 2.5 days later, the upwelled end member appeared at WG, and then slow relaxation followed, with the inner bay water appearing at the the location 7 days later (**Figure 20A**). At F10, the initial water mass was the inner bay end member (**Figure 20B**). The upwelled water appeared at F10 in 3 days, and then another 4 days followed before F10 returned to its initial state (**Figure 20B**). The water masses at each station were identified by comparing their temperature and salinity signatures to the position on the mixing lines observed from the wave glider (**Figure 21**).

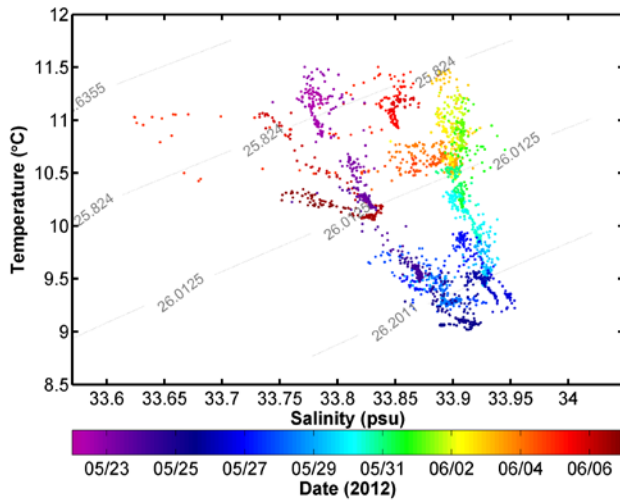


Figure 19: TS plot with density contours at the M1 station from May 22 to June 7, with date shown on the color axis.

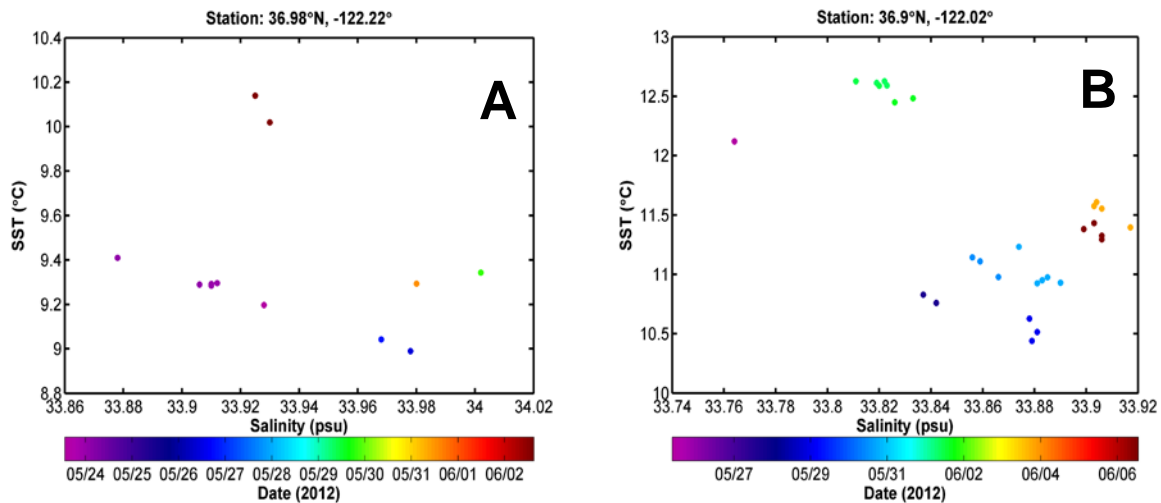


Figure 20: TS plot at stations WG (A) and F10 (B). Data were from repeat occupations of the location by the wave glider, with the date of occupation shown on the color axis. Note that the two color axes do not show the same dates.

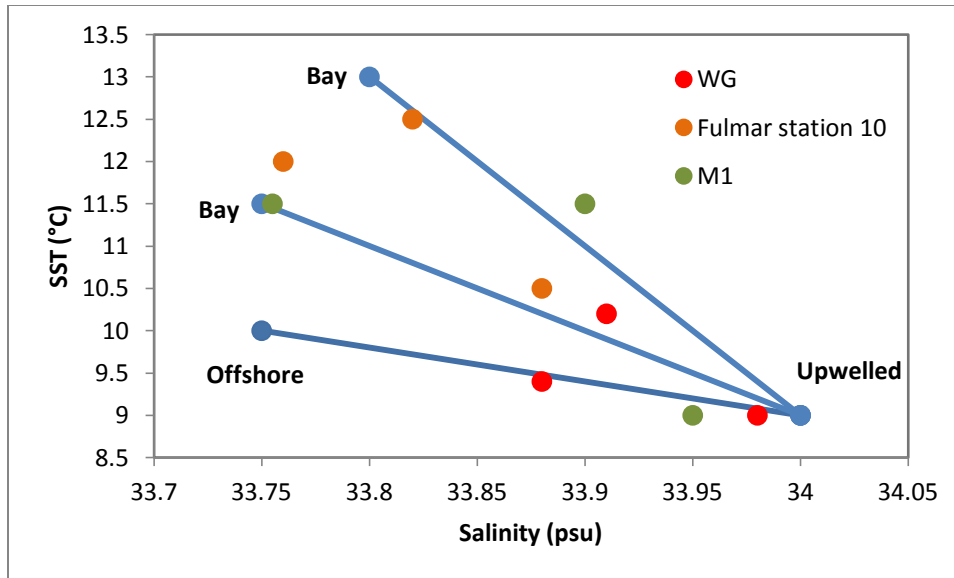


Figure 21: Schematic TS plot showing the three end members (bay, offshore, and upwelled waters) and the mixing lines observed from the wave glider. The end members observed from the stations WG, F10, and M1 were also plotted for comparison.

Because salinity was a conservative tracer over the observation period, plots of sea $p\text{CO}_2$, pH, and O_2 also showed the same pattern of mixing (**Figures 22-23**). The inner bay water was characterized by low $p\text{CO}_2$ (200 μatm), high pH (8.2), and high O_2 (350 μM); the offshore water had moderate pH (7.88), $p\text{CO}_2$ (700 μatm), and O_2 (250 μM); and the upwelled water had the highest $p\text{CO}_2$ ($> 1000 \mu\text{atm}$), lowest pH (7.6), and lowest O_2 (200 μM) (**Figures 22-23**). Whereas in the TS plot, the slope of the upwelled-inner bay water mixing line increased over time with the warming of temperatures and increase in salinity of the water masses, this effect was not seen in $p\text{CO}_2$, pH, and O_2 , which all lied on the same mixing lines (**Figures 17A, 22-23**). Despite the general temperature dependence of $p\text{CO}_2$, pH, and O_2 (higher $p\text{CO}_2$, lower pH, and lower O_2 with increasing temperatures), temperature had little effect on these parameters during the gradual warming of waters during relaxation. For instance, the $p\text{CO}_2$, pH, and O_2 signature of the inner bay water remained relatively constant for a warming from 11.5 to 13.5°C (**Figures 22-23**). Although pH and O_2 exhibited linear mixing lines (**Figures 22B, 23**), $p\text{CO}_2$ versus salinity had a slightly non-linear relationship unless plotted on a semilog scale (**Figure 22A**), due to the non-linear relationship between $p\text{CO}_2$ and pH (which is on a logarithmic scale).

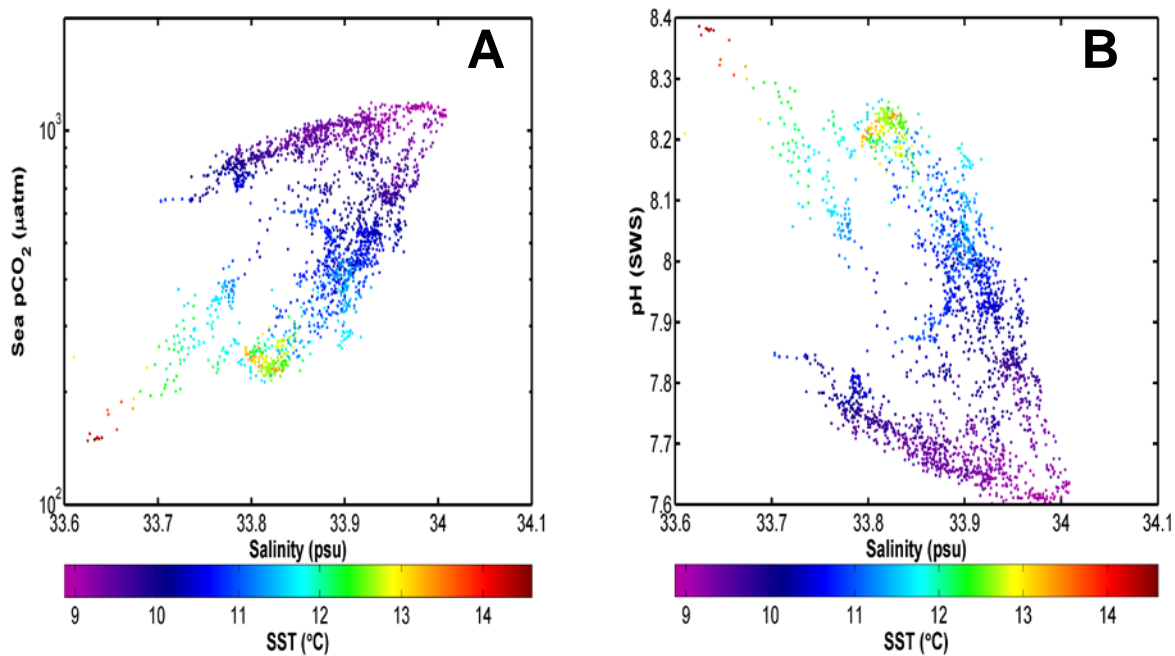


Figure 22: (A) Wave glider sea pCO₂ versus salinity. pCO₂ is on a log axis. (B) Wave glider pH versus salinity. SST is on the color axis in both scatter plots.

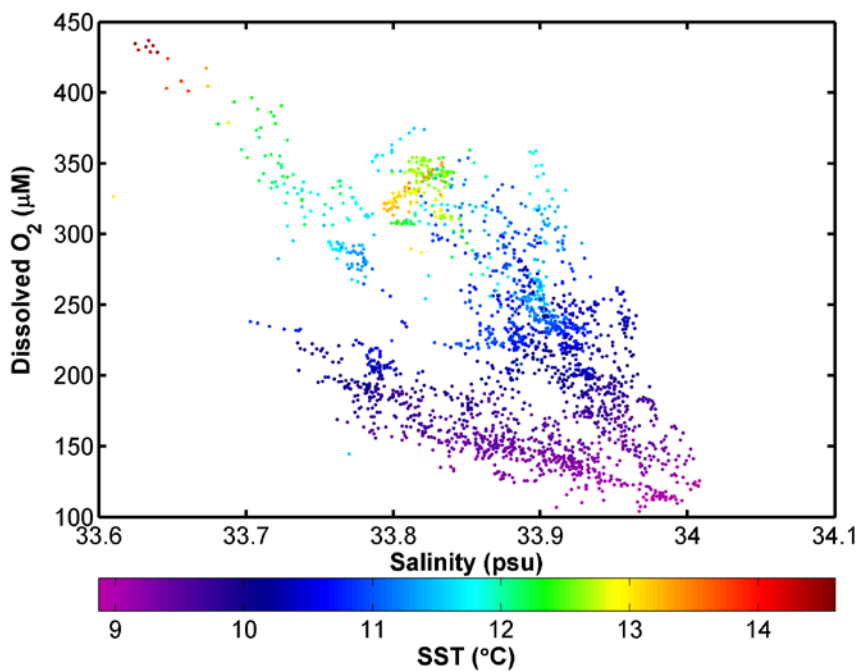


Figure 23: Wave glider dissolved O₂ versus salinity, with SST on the color axis.

CO₂ AND O₂ FLUX:

The CO₂ and O₂ versus salinity plot with the sea to air flux on the z-axis (**Figure 24**) shows the flux associated with a particular water mass. **Figure 24** reveals several important features of the CO₂ and O₂ fluxes. (1) The predominant direction of flux during the observation period was into the ocean for O₂ and into the atmosphere for CO₂. (2) O₂ fluxes are three orders of magnitude greater than CO₂ fluxes (mol m⁻² d⁻¹ vs. mmol m⁻² d⁻¹). (3) The largest fluxes occurred in the upwelling or offshore region, and (4) the strong fluxes were short-lived (a few days), as they lied mostly along the mixing line between the upwelled and offshore end members (May 22-May 26).

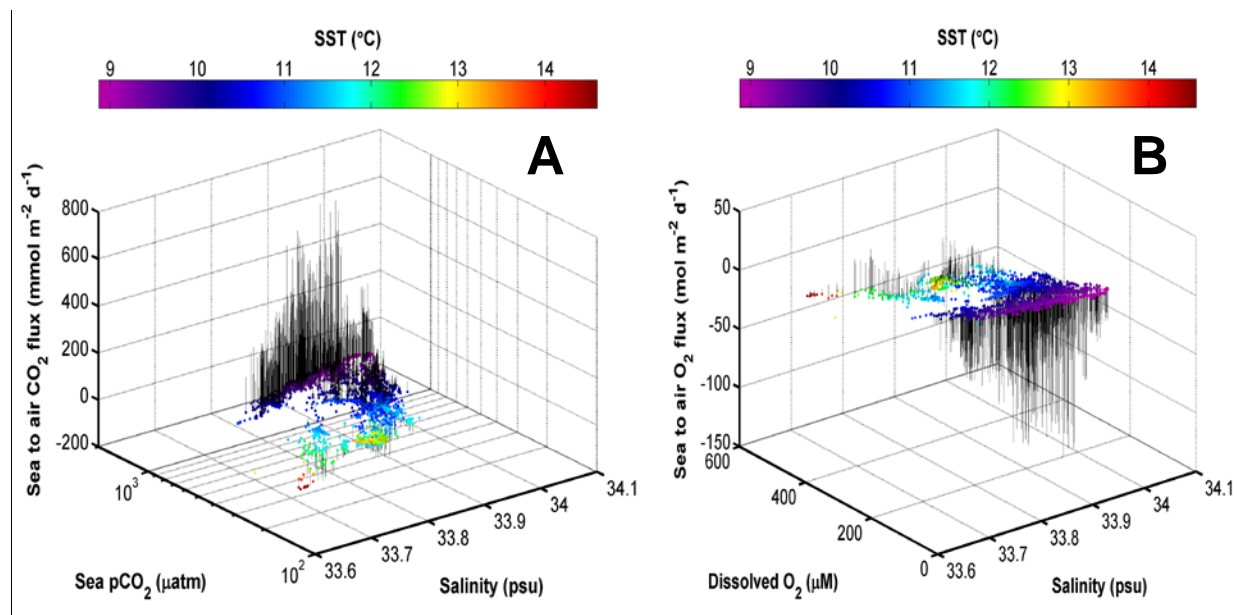


Figure 24: (A) Wave glider sea pCO₂ versus salinity (semilog plot) with SST on the color axis and CO₂ flux (mmol m⁻² d⁻¹), depicted by vertical stems, on the z-axis. Fluxes from sea to air are positive with stems pointing up. (B) The same type of plot for oxygen. Oxygen fluxes are in mol m⁻² d⁻¹.

Surface maps of the fluxes also showed the short-lived nature of the strong fluxes (**Figures 5-14**). The strongest fluxes (800 mmol m⁻² d⁻¹ for CO₂ and -150 mol m⁻² d⁻¹ for O₂) occurred during leg 2 when the strongest winds (>20 m/s) were observed, and pCO₂ levels were above 1000 µatm (and O₂ concentrations at the minimum of 100 µM). By leg 4 (**Figure 8**), O₂ and CO₂ fluxes have already died down to mostly zero, and the near zero fluxes persisted until the end of the observation period.

METHOD VALIDATION:

Agreement of wave glider measurements across multiple platforms validated the method. Calibration of wave glider pCO₂ against M1 pCO₂ yielded excellent linear correlation ($R^2=0.9966$), with a slope of $m=1.0012$ (**Figure 25**). Comparison of pCO₂ in a temperature and salinity space also yielded excellent agreement. The wave glider and the M1 station agreed for pCO₂ versus salinity, and the wave glider, M1 station, and the Fulmar underway pCO₂ system agreed for pCO₂ versus temperature (**Figure 26**).

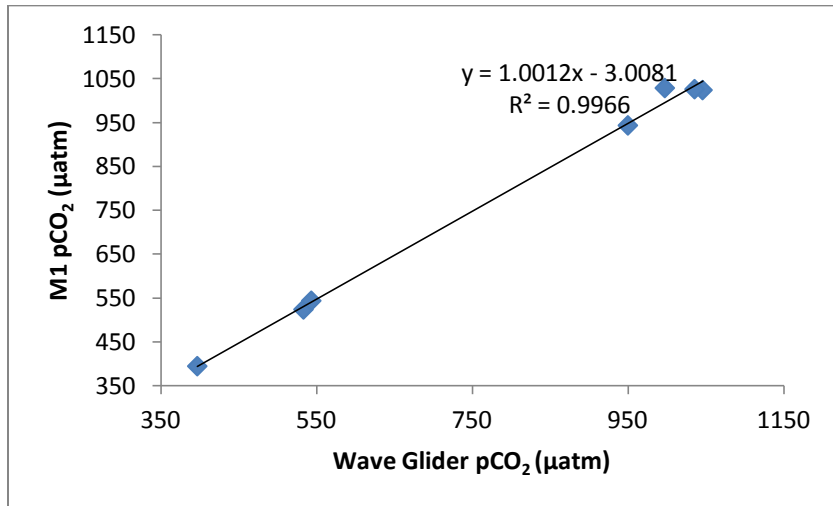


Figure 25: pCO₂ measured at M1 at a depth of 1 m versus surface pCO₂ measured by the wave glider for instances when the wave glider was less than 4 km away from M1 and for measurements less than 4 minutes apart.

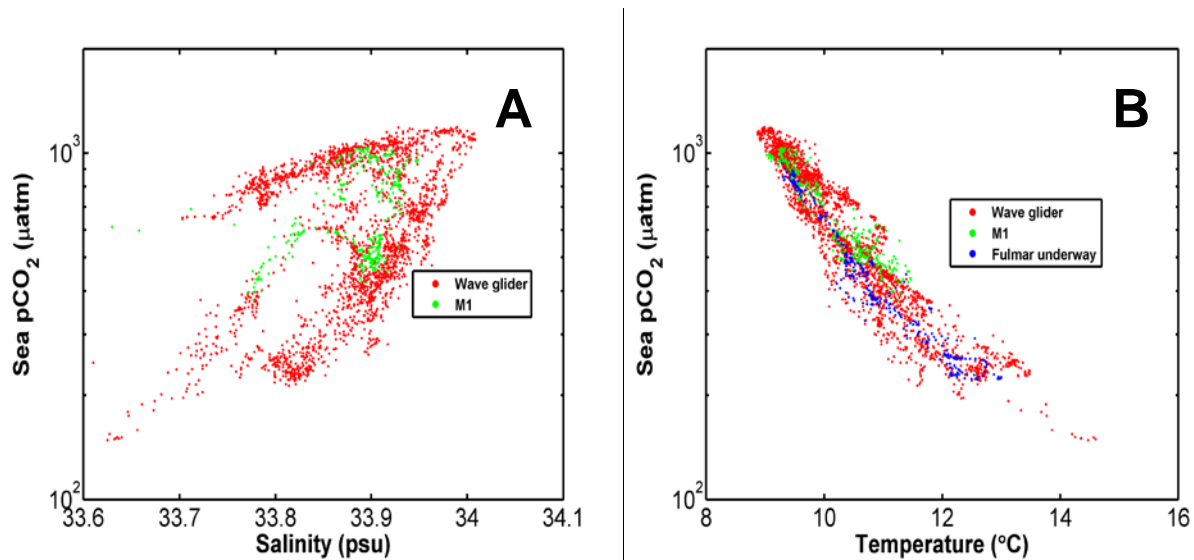


Figure 26: Sea pCO₂ versus salinity from the wave glider and M1 station (A) and versus temperature (B) from the wave glider, M1, and Fulmar underway pCO₂ system.

Further evidence strengthening the comparisons of $p\text{CO}_2$ in a temperature and salinity space is the agreement of temperature and salinity across four different platforms. Overlaid TS plots from the wave glider, Fulmar profiling CTD (for depths < 20 m), the *Dorado* AUV (for depths < 20 m), and the M1 station (at 1 m), over the same observation period, showed the same envelope of temperature and salinity values, demonstrating that the same water masses were observed and that comparisons of $p\text{CO}_2$ measurements were among the same water masses (**Figure 27**).

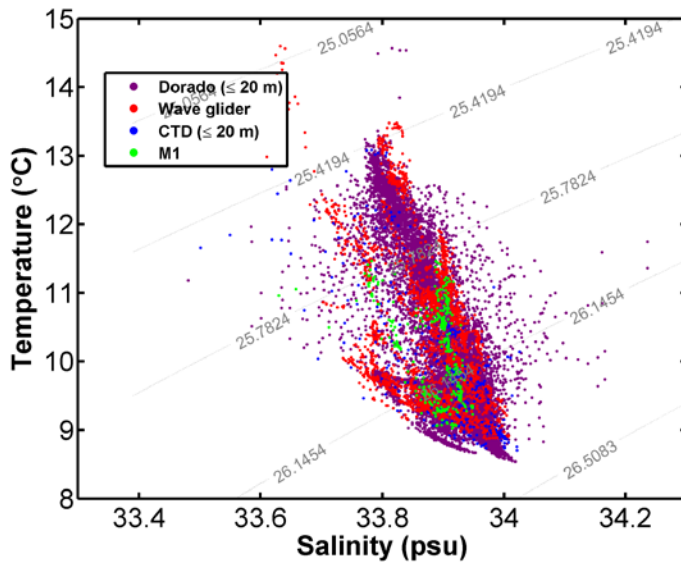


Figure 27: Overlaid TS plots, with density contours, from the *Dorado* AUV (for depths ≤ 20 m), the wave glider, the Fulmar profiling CTD (for depths ≤ 20 m), and the M1 mooring station (at 1 m depth). Data from the different platforms were filtered to be within the same observation period and latitude/longitude range.

DISCUSSION

REGULATING PROCESSES ON SEA SURFACE $p\text{CO}_2$:

The gradual decay of sea surface $p\text{CO}_2$ to atmospheric levels (and below) during the relaxation of upwelling may have been influenced by multiple processes. As seen in the $p\text{CO}_2$ versus salinity diagram (**Figure 22A**), mixing of different water masses can change $p\text{CO}_2$. In **Figure 22A**, atmospheric or sub-atmospheric $p\text{CO}_2$ may be obtained by mixing between the upwelled and inner bay end members. The well-defined mixing lines in **Figure 22A** provide evidence that mixing and advection were important in determining the sea surface $p\text{CO}_2$.

Because of the stimulation of phytoplankton blooms by the upwelling of nutrient-rich waters, the biological uptake of CO₂ by photosynthesis was naturally expected to be a significant factor in drawing down sea surface pCO₂ during the relaxation of upwelling. Chlorophyll profiles from bottle data indeed showed a significant growth at the surface during relaxation (**Figures 28**).

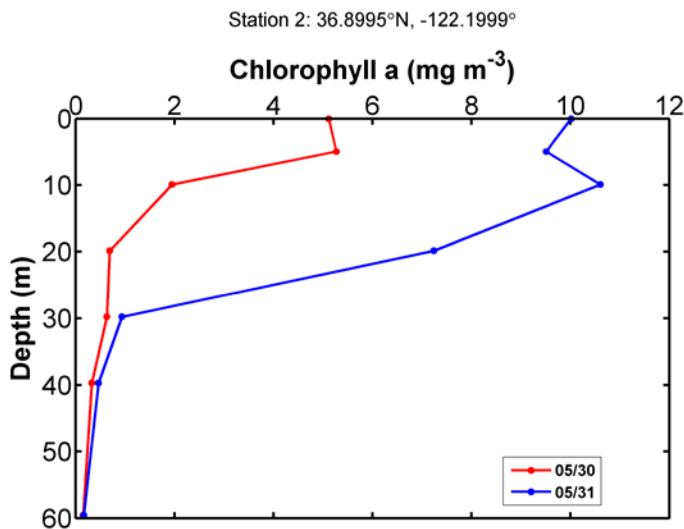


Figure 28: Chlorophyll a profiles from bottle data at the Fulmar CTD station 2 with profiles taken on two different days. The surface chlorophyll shows the growth of phytoplankton during the relaxation period.

The sea to air flux of CO₂ could also potentially have significant impact on the surface sea pCO₂, but the strong fluxes were short-lived (on the order of days). Strong fluxes were observed initially due to the strong winds and high sea pCO₂ in the upwelling region, but then quickly weakened with the winds.

MODEL SIMULATIONS OF pCO₂ DECAY:

Station WG, the origin of the upwelled water, had the highest pCO₂ observed during the study period (>1000 μatm) and a strong initial sea to air CO₂ flux (**Figures 6-7**). To assess if the strong initial fluxes alone could bring sea pCO₂ back to atmospheric levels or below, the model simulation with no biology (zero growth rate) was performed at WG. Over the course of seven days, the length of observations at WG, sea pCO₂ decreased from 1150 μatm to 800 ppm in 4 days and then remained constant at 800 μatm for the rest of the simulation (**Figure 29A**). Gas

exchange alone was insufficient in drawing down sea pCO₂ back to atmospheric levels, because the strong CO₂ fluxes did not persist long. O₂ was not the main focus of this study and was not incorporated into the model, but it may be noteworthy that the O₂ fluxes were into the ocean and were three order of magnitudes greater than CO₂ fluxes (**Figure 24**). It may be possible that gas exchange has a significant effect on dissolved O₂. Model simulations of O₂ are needed to test this suspicion.

With a constant, low growth rate (assumed to be $\mu=0.3\text{ d}^{-1}$, since the outer bay regions are lower in productivity than the inner bay), sea pCO₂ decayed to atmospheric levels in 12 days and to 250 μatm (inner bay levels) in 15 days (**Figure 29B**). Lower pCO₂ levels could not be attained, because nitrate was completely depleted after 14 days (**Figure 29B**). Only 17% of the cumulative change in dissolved inorganic carbon (dTCO₂) was due to gas exchange (atmospheric loss), when bringing down sea pCO₂ from 1150 μatm to 250 μatm (**Figure 29B**). 83% of the cumulative change in DIC was due to the biological uptake CO₂. Overall, biology had a stronger influence than strong, but short-lived air-sea gas fluxes on sea pCO₂, ultimately being responsible for pushing sea pCO₂ below atmospheric levels, but in the earlier stages of relaxation (first 4 days), when the standing biomass was low, gas exchange comprised up to 100% of the cumulative change in DIC.

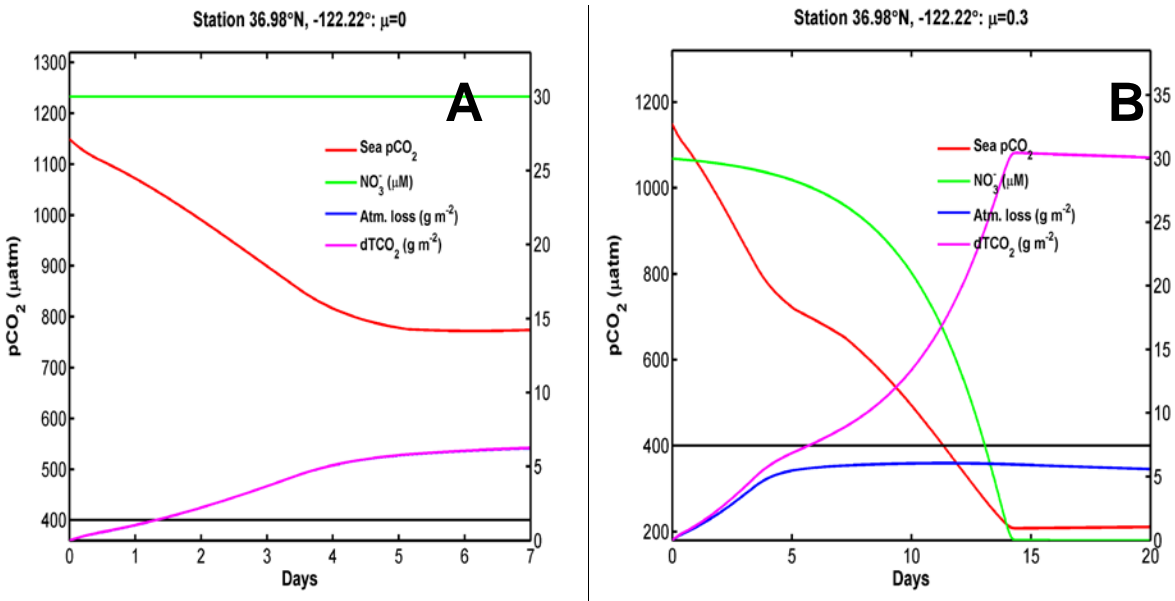


Figure 29: (A) Model simulation of pCO₂ decay at station WG in a pure gas exchange, no biology (zero growth rate) scenario. (B) Simulated pCO₂ decay with a constant, low growth rate of $\mu=0.3\text{ d}^{-1}$ and all other conditions the same. The black bar shows atmospheric pCO₂ (400 μatm).

The constant biology scenario at the other three stations yielded similar results. Biological uptake comprised an increasingly significant fraction of $d\text{TCO}_2$ with time and ultimately became the strongest factor in sea $p\text{CO}_2$ decay. With higher growth rates and/or weaker CO_2 flux, gas exchange became insignificant even in the initial stage of relaxation (Figures 30A, 30B).

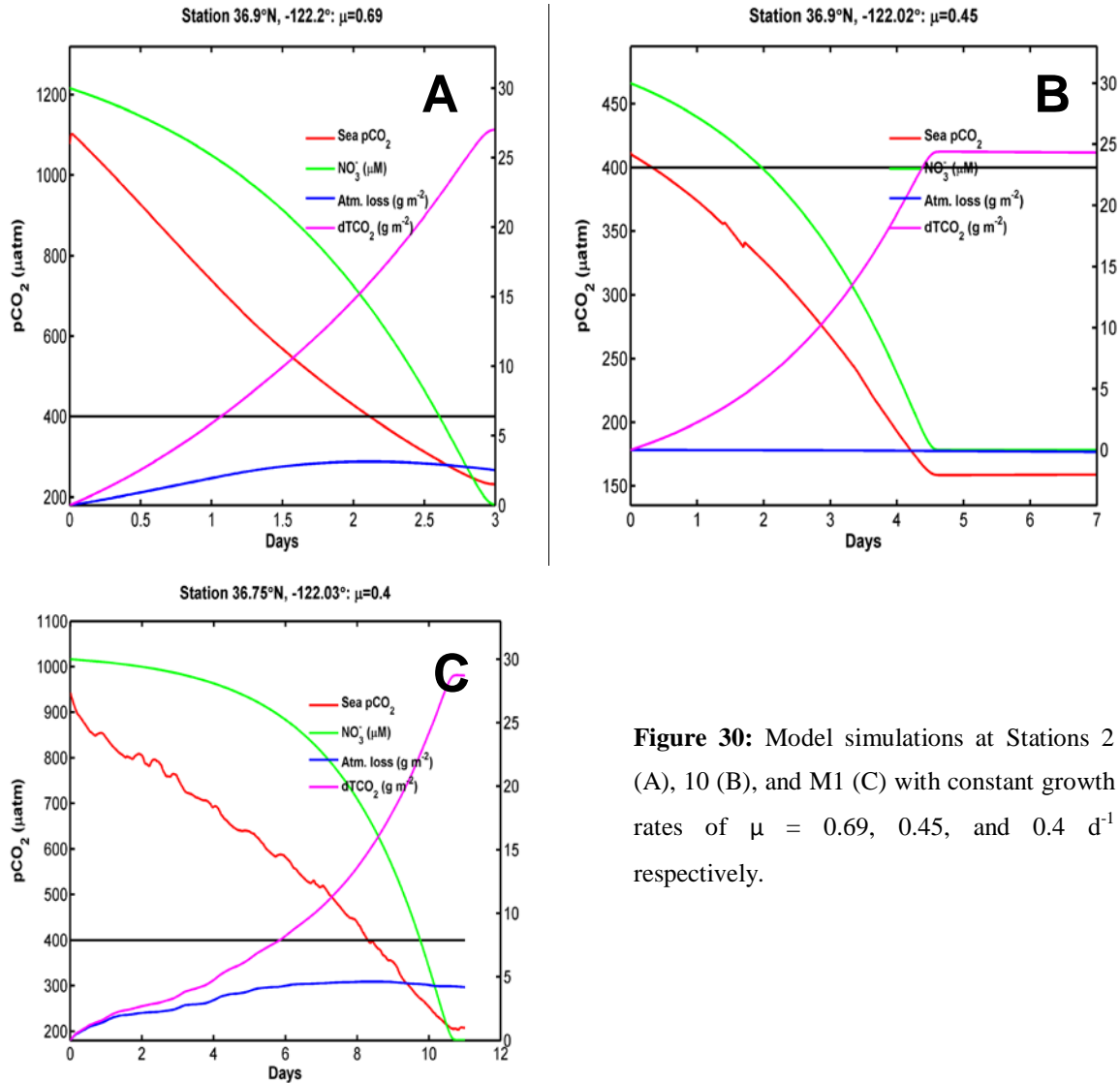


Figure 30: Model simulations at Stations 2 (A), 10 (B), and M1 (C) with constant growth rates of $\mu = 0.69$, 0.45 , and 0.4 d^{-1} respectively.

ADVECTIVE TIMESCALES VS. MODELED DECAY TIMESCALES:

Although the model simulations were insightful in revealing the relative contributions of biology and gas exchange to the decay of sea pCO₂ during upwelling relaxation, the model assumes no advection, which could potentially be as important as the other processes. From analysis of the TS plots at each of the stations (**Figures 19-20**), advective timescales could be inferred from the time between the appearances of the three major water masses at a station. If the time for gas exchange and biology to decay sea pCO₂ from the high upwelled levels to atmospheric (400 μatm) or inner bay levels (≤ 250 μatm) is significantly quicker than the time required to replace the upwelled water with low pCO₂ water, then the pCO₂ would be persistently low. However, if the advective timescale is quicker than the modeled decay timescale, then the pCO₂ should be persistently higher than inner bay levels, because the mixing of two water masses would yield pCO₂ levels intermediate to the two end members.

Figure 31 summarizes the comparison of advective and modeled decay timescales. The advection of upwelled water southwards and into the bay was relatively quick, taking 3 days. Relaxation was slow, taking at least a week for the inner bay waters to expand back into the outer bay and offshore areas (**Figure 31**). In the inner bay station, F10, sea pCO₂ was persistently low (200 μatm, **Figures 5-14**), because the decay timescale was very quick compared to the advective timescale. Even at the peak of upwelling (**Figure 7**), F10 maintained low sea pCO₂. From **Figure 31**, 3 days was required to bring the upwelled water to F10, but only 0.3 days was required to decay sea pCO₂ to atmospheric levels and 3 days to reach 250 μatm. Therefore, the highest sea pCO₂ attained at F10 was only slightly above 400 μatm. Another factor that maintained the low pCO₂ at F10 was the quick advection (4 days) of low pCO₂ water into the area from waters further within the inner bay. In the outer bay stations, WG and M1, the modeled decay timescales were much slower (longer than a week), while the advective timescales (replacement with inner bay water) were also on the same order (**Figure 31**). Because of the slow decay of pCO₂ and the constant, gradual mixing with the inner bay waters, WG and M1 maintain a sea pCO₂ that is higher than in the inner bay.

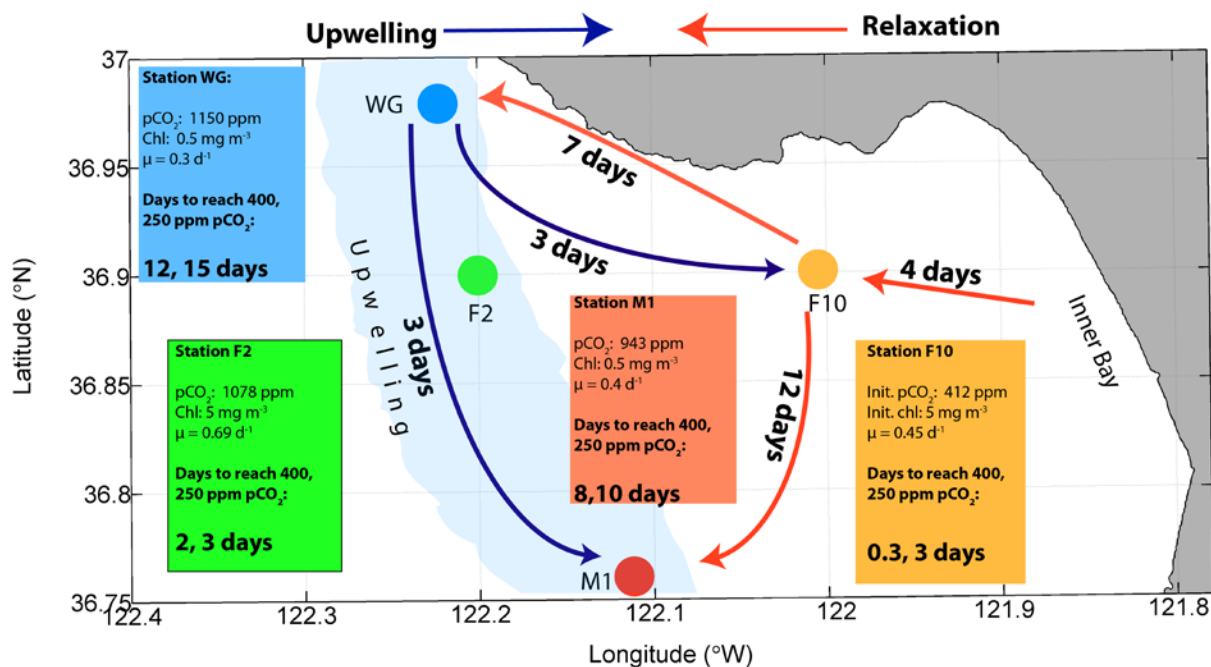


Figure 31: Summary schematic of the comparative analysis of modeled pCO₂ decay timescales and advective timescales. The boxes show the model results at each station: initial conditions, growth rates, and the time to reach 400 and 250 μatm sea pCO₂. The blue arrows show the time required for the upwelled water to travel from the source (at Station WG) to the other stations. The red arrows show the time required for the inner bay water to travel to the other stations during the relaxation of upwelling. Arrows do not denote actual path of the water.

CONCLUSIONS

The wave glider platform was an effective instrument in making a variety of surface measurements at a high spatiotemporal resolution and revealing surface processes. Comparison of data across multiple platforms showed that wave glider pCO₂ measurements were comparable to measurements made from mooring stations or ship underway systems. The agreement provided confidence that surface sea pCO₂ can be studied reliably with the wave glider platform. The deployment of the wave glider in the Monterey Bay over the course of two weeks allowed for the mapping of surface parameters (temperature, salinity, pH, O₂, and pCO₂) and also captured the spatial and time evolution of surface hydrography and chemistry during upwelling and relaxation. Sharp spatial and temporal gradients in chemistry were observed—for instance, sea pCO₂ gradients up to 600 μatm were seen over a distance of 4 km and also over the course of

hours. The richness of the data obtained from the wave glider attest to its capability in capturing the surface variability and fast oceanographic processes.

From the wave glider observations, several important features and processes of upwelling and relaxation were characterized. The wave glider's built-in weather station was invaluable in determining the air-sea CO₂ and O₂ flux from instantaneous winds, which were highly variable in space and time, and especially in areas of strong winds (>20 m/s), where ship observations are sparse and impractical. The strongest CO₂ and O₂ fluxes were observed during upwelling, with the strongest wind speeds and the greatest air-sea difference in CO₂ and O₂. Wave glider CTD measurements revealed a mixing regime between three distinct water masses: cold, low salinity offshore water; cold, saline upwelled water; and warm, low salinity inner bay water. The high spatiotemporal density of the measurements also captured the intermediate products of mixing and the time evolution of the water masses. Salinity was a conservative tracer, and chemical parameters (pH, pCO₂, and O₂) were a function of salinity due to conservative mixing. The wave glider was also capable of functioning as a virtual mooring station. Hydrographic and chemical parameters at three selected positions (WG, F2, F10) along the wave glider track showed the same mixing regime and water masses and allowed the rough determination of advective timescales, based on the transit time between different water masses.

The dynamics of surface sea pCO₂ in the Monterey Bay were complicated by a combination of gas exchange, advective mixing, and biology. Model simulations of the sea pCO₂ decay due to gas exchange and biology showed that strong, but short-lived CO₂ fluxes alone could not bring pCO₂ down to atmospheric levels or below. Overall, biology comprised the largest fraction of the cumulative change in DIC, but during the initial stages of relaxation, gas exchange can be significant. In the inner bay, where the timescale of decay of sea pCO₂ by gas exchange and biology was much quicker than the advective replacement of the low pCO₂ water with high pCO₂ upwelled water, sea pCO₂ remained persistently low (as low as 200 μatm). The outer bay region never attained the below atmospheric pCO₂ levels seen in the inner bay, because the advective replacement and pCO₂ decay timescales were similar. Future studies can better characterize the advective timescales and test the results of the model.

The wave glider observations and the model simulations of sea pCO₂ decay provided some preliminary insights on the dynamics of upwelling and the pCO₂ system in the Monterey

Bay. The source of the upwelled water is from a depth of 30-50 m and originates from north of the Monterey Bay. The cold, high salinity, and high $p\text{CO}_2$ upwelled water is quickly advected southwards and also into the bay within a few days. A slow relaxation process then proceeds over the course of up to two weeks and involves the expansion of the inner bay waters outwards. Slow, widespread warming of the waters occurs, and salinity also increases as the upwelled water is mixed throughout the bay. The dynamics of the surface sea $p\text{CO}_2$ system during upwelling process is summarized in the conceptual model in **Figure 32**. The highest sea $p\text{CO}_2$ is found within the upwelling plume, while the lowest $p\text{CO}_2$ persists in the inner bay. In the initial stages of upwelling, sea $p\text{CO}_2$ remains high along the upwelling plume, because of low primary productivity in the region, while low $p\text{CO}_2$ persists in the inner bay despite the advection of the high $p\text{CO}_2$ upwelled water into the area, because of high primary productivity and thus fast biological uptake of CO_2 . Strong winds and strong CO_2 fluxes are characteristic of the upwelling stage, and both die down significantly by the end of the relaxation. During relaxation, the low $p\text{CO}_2$ water slowly migrates offshore and mixes with higher $p\text{CO}_2$ water. At the end of relaxation, the sea $p\text{CO}_2$ in the outer bay region is mostly at moderate or atmospheric levels due to a combination of mixing with low $p\text{CO}_2$ inner bay waters, biological uptake, and gas exchange.

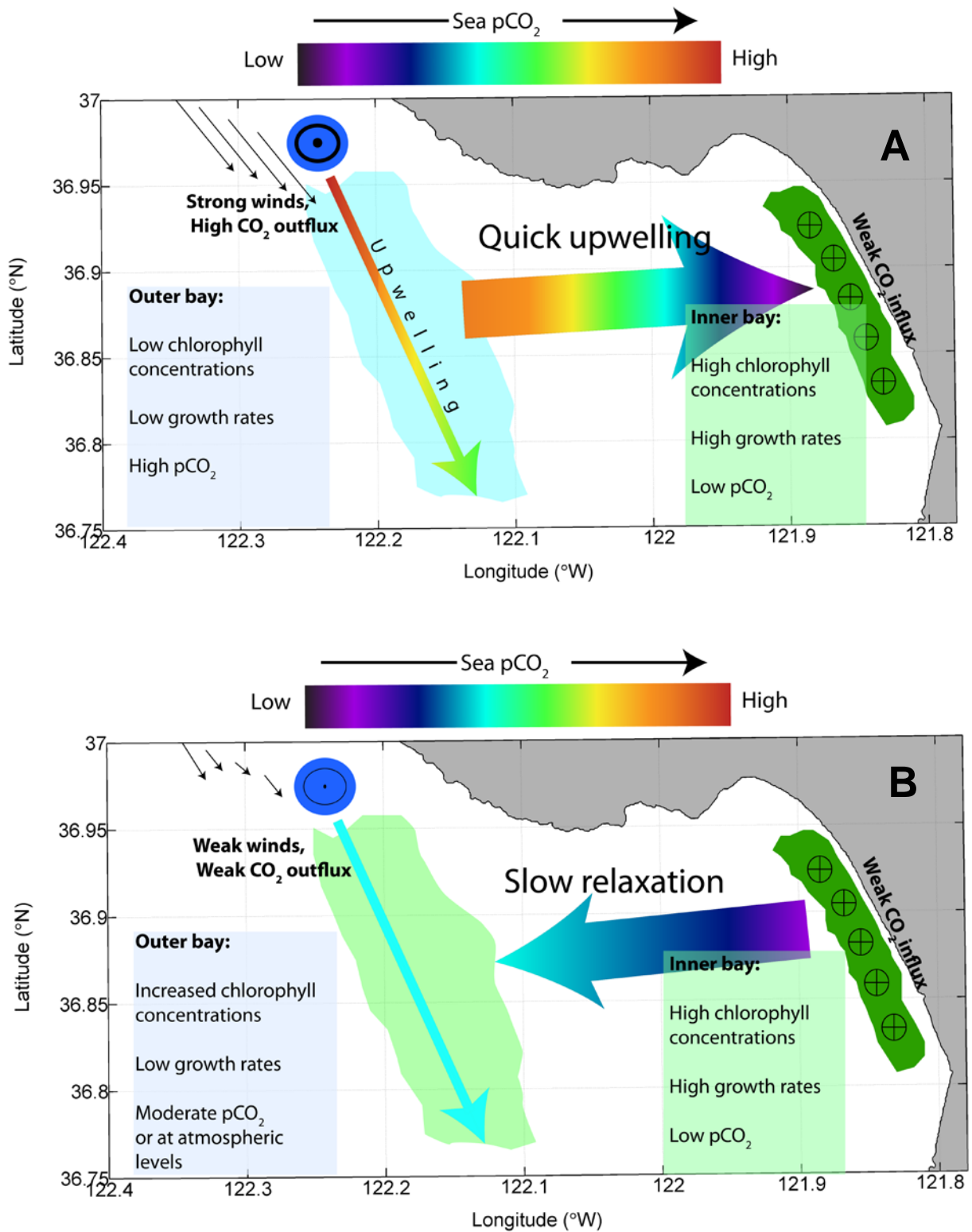


Figure 32: Conceptual model of the dynamics of surface sea pCO₂ and the physical and biological characteristics of the Monterey Bay during the beginning of upwelling (A) and the end of relaxation (B).

ACKNOWLEDGEMENTS

First, I would like to thank the ITD Department at MBARI, which funded the internship program, and George Matsumoto and Linda Kuhnz for taking such good care of the interns, arranging events and opportunities for us, and going out their way to keep everyone happy. For my project and the incredible learning experience I had at MBARI, I have my mentors Francisco Chavez and Gernot Friederich to thank. My fellow lab members in the Biological Oceanography group were also wonderful, helpful, and supportive. Thanks especially to Jules Friederich, for introducing me to instrumentation programming with Agilent VEE and getting me to dabble briefly in a side project, and to Reiko Michisaki for always being quick to help when needed. And lastly, my fellow interns helped make the internship a great experience. Dongsik Chang and Francisco Lopez were especially helpful whenever I had questions about MATLAB or Ocean Data View.

References:

- Dickson, A.G. (1990). Standard potential of the reaction: $\text{AgCl(s)} + 1/2\text{H}_2(\text{g}) = \text{Ag(s)} + \text{HCl(aq)}$, and the standard acidity constant of the ion HSO_4^- in synthetic seawater from 273.15 to 318.15 K. *Journal of Chemical Thermodynamics*, **22**:113-27.
- Eppley, R.W., Peterson B.J. (1979). Particulate organic matter flux and planktonic new production in the deep ocean. *Nature*, **282**, 677-680.
- Friederich, G.E., Brewer, P.G., Herlien, R., Chavez, F.P. (1995). Measurement of sea surface partial pressure of CO_2 from a moored buoy. *Deep Sea Research I*, **42**, 1175-1186.
- Large, W.G., Pond, S. (1981). Open ocean momentum flux measurements in moderate to strong winds. *Journal of Physical Oceanography*, **11**: 324-336.
- Manley, J., Willcox, S. (2010). The Wave Glider: A persistent platform for ocean science. *OCEANS 2010 IEEE - Sydney* 1-5. doi: 10.1109/OCEANSSYD.2010.5603614
URL: <http://ieeexplore.ieee.org/stamp/stamp.jsp?tp=&arnumber=5603614&isnumber=5603506>
- Monteiro, P.M.S., Schuster, U., Hood, M., Lenton, A., Metzl, N., Olsen, A., Rogers, K., Sabine, C., Takahashi, T., Tilbrook, B., Yoder, J., Wanninkhof, R., Watson, A.J. (2009). A global sea surface carbon observing system: Assessment of changing sea surface CO_2 and air-sea CO_2 fluxes. OceanObs' 09 Conference. URL: <http://www.oceanobs09.net/proceedings/cwp/>
- Roy, R.N., Roy, L.N., Vogel, K.M., Porter-Moore, C., Pearson, T., Good, C.E., Millero, F.J., Campbell, D.M. (1993). The dissociation constants of carbonic acid in seawater at salinities 5 to 45 and temperatures 0 to 45°C. *Marine Chemistry* **44**:249-267.

- Schlitzer, R. (2011). Ocean Data View. URL: <http://odv.awi.de>
- Takahashi, T., Olafsson, J., Goddard, J.G., Chipman, D.W., Sutherland, S.C. (1993). Seasonal variation of CO₂ and nutrients in the high-latitude surface oceans: A comparative study. *Global Biogeochemical Cycles*, **7**, 843-878.
- Tougher, B. (2011). Wave Glider @ ASV ocean acidification sensor integration for marine management applications. MBARI summer internship report.
- van Heuven, S., Pierrot, D., Rae, J.W.B., Lewis, E., Wallace, D.W.R. (2011). MATLAB Program Developed for CO₂ System Calculations. ORNL/CDIAC-105b. Carbon Dioxide Information Analysis Center, Oak Ridge National Laboratory, U.S. Department of Energy, Oak Ridge, Tennessee. doi: 10.3334/CDIAC/otg.CO2SYS_MATLAB_v1.1
- Wanninkhof, R. (1992). Relationship between wind speed and gas exchange over the ocean. *Journal of Geophysical Research*, **97**: 7373-7382.
- Weiss, R.F., Price, B.A. (1980). Nitrous oxide solubility in water and seawater. *Marine Chemistry*, **8**, 347-359.
- Willcox, S., Meinig, C., Sabine, C.L., Lawrence-Slavas, N., Richardson, T., Hine, R., Manley, J. (2009). An autonomous mobile platform for underway surface carbon measurements in open-ocean and coastal waters. *OCEANS 2009, MTS/IEEE Biloxi - Marine Technology for Our Future: Global and Local Challenges*, 1-8, URL: <http://ieeexplore.ieee.org/stamp/stamp.jsp?tp=&arnumber=5422067&isnumber=5422059>
- Wolf-Gladrow, D.A., Zeebe, R.E., Klaas, C., Kortzinger, A., Dickson, A.G. (2007). *Marine Chemistry*, **106**, 287-300.
- MBARI (2010). CANON: Controlled, Agile, and Novel Observing Network. URL: <http://www.mbari.org/canon/>
- Liquid Robotics. Wave glider advantages. URL: <http://liquidr.com/technology/wave-glider-advantages/>